A geometry conforming isogeometric method for the self-adjoint angular flux (SAAF) form of the neutron transport equation with a discrete ordinate (S_N) angular discretisation

C. Latimer[a], J. Kópházi[a], M. D. Eaton[a], R. G. McClarren[b]

[a]*Nuclear Engineering Group*
Department of Mechanical Engineering, Imperial College London
City and Guilds Building, Exhibition Road, South Kensington Campus, SW7 2AZ
[b]*Department of Aerospace and Mechanical Engineering University of Notre Dame*
Fitzpatrick Hall, Notre Dame, IN 46556

Abstract

This paper presents the application of isogeometric analysis (IGA) to the spatial discretisation of the multi-group, self-adjoint angular flux (SAAF) form of the neutron transport equation with a discrete ordinate (S_N) angular discretisation. The IGA spatial discretisation is based upon non-uniform rational B-spline (NURBS) basis functions for both the test and trial functions. In addition a source iteration compatible maximum principle is used to derive the IGA spatially discretised SAAF equation. It is demonstrated that this maximum principle is mathematically equivalent to the weak form of the SAAF equation. The rate of convergence of the IGA spatial discretisation of the SAAF equation is analysed using a method of manufactured solutions (MMS) verification test case. The results of several nuclear reactor physics verification benchmark test cases are analysed. This analysis demonstrates that for higher-order basis functions, and for the same number of degrees of freedom, the FE based spatial discretisation methods are numerically less accurate than IGA methods. The difference in numerical accuracy between the IGA and FE methods is shown to be because of the higher-order continuity of NURBS basis functions within a NURBS patch as well as the preservation of both the volume and surface area throughout the solution domain within the IGA spatial discretisation. Finally, the numerical results of applying the IGA SAAF method to the OECD/NEA, seven-group, two-dimensional C5G7 quarter core nuclear reactor physics verification benchmark test case are presented. The results, from this verification benchmark test case, are shown to be in good agreement with solutions of the first-order form as well as the second-order even-parity form of the neutron transport equation for the same order of discrete ordinate (S_N) angular approximation.

1. Introduction

Second-order forms of the neutron transport equation, such as the even-parity (EP) and self-adjoint angular flux (SAAF) equation, have been investigated since the mid 1960s [1, 2]. They

Email address: c.latimer15@imperial.ac.uk (C. Latimer)

have a number of numerical advantages over the first-order form of the neutron transport equation. One of the key numerical advantages of second-order forms is that they are numerically stable when spatially discretised using a continuous Bubnov-Galerkin discretisation using prescribed test and trial functions. Conversely, the first-order form of the neutron transport equation can produce spurious numerical artefacts, near sharp gradients in the solution, when discretised using the same approach [3]. Therefore, in general, the first-order form has to be discretised using either stabilised FE methods such as streamlined-upwind Petrov-Galerkin (SUPG) or discontinuous Galerkin methods [4, 5]. The use of discontinuous Galerkin methods can lead to significantly more degrees of freedom than the equivalent continuous Bubnov-Galerkin discretisation [6, 7].

A further advantage of second-order forms of the neutron transport equation (such as the SAAF and the EP equations) are that they produce symmetric positive definite (SPD) systems of linear equations when their weak form is spatially discretised using a Bubnov-Galerkin approach. SPD linear systems of equations can be solved efficiently with preconditioned conjugate gradient matrix solution algorithms [8]. Amongst the second-order forms of the neutron transport equation the most widely used are the EP, self-adjoint angular flux (SAAF), and symmetrised neutron transport (ST) [9] forms. Such forms, of the neutron transport equation, have been used extensively because they are self-adjoint equations and extremum variational principles may be derived for them [2] which allows for upper and lower bounds of the solution to be determined [10]. The EP form of the neutron transport equation allows for the efficient computation of the scalar neutron flux. The efficiency of the EP form is due to the number of angular unknowns being approximately half of that required by the SAAF or the first-order form of the neutron transport equation. Nevertheless, the additional cost of the SAAF solution provides the full angular neutron flux which, amongst other things, allows for easier implementation of S_N reflective boundary conditions [11].

A disadvantage of the aforementioned second-order forms is that they are unable to model voided regions whilst maintaining symmetry of the system and global conservation of neutrons. The least-squares (LS) formulation [12] developed by Hansen et. al. is symmetric but does not maintain conservation of neutrons except in the limit of the discretisation error vanishing. The hybrid SAAF & conservative LS (SAAF-CLS) formulation by Laboure et. al. [13] maintains conservation of neutrons and can model near-void regions, but is not symmetric. Void treatments for the SAAF form of the neutron transport equation have similar issues [11, 14]. Zheng et. al. presented a sub-domain discontinuous least-squares scheme (SDLS) that is globally continuous and forms a symmetric system of linear equations within each sub-domain. However, the sub-domain problems have to be linked together using transport sweeps or solved simultaneously as a non-symmetric global system of equations [15].

The SAAF equation was first derived from a variational principle by Pomraning and Clark [2]. However, this was only for one-dimensional (1D) slab geometries where the material cross-sections are spatially constant. Later, Ackroyd derived a more general three-dimensional (3D) maximum principle for the SAAF equation from his $\tilde{K}$ functional without any restriction on the spatial variation in the macroscopic neutron cross-sections [16]. Morel & McGhee published the first detailed theoretical and numerical study of the SAAF equation. Their paper presented a source iteration suitable formulation and also considered the relative advantages and disadvantages when compared to the first-order form and the EP & OP forms of the neutron transport equation [11]. In their paper they provided a simple algebraic derivation of the SAAF equation and spatially discretised it using a lumped FE approach. They utilised a discrete ordinate S_N angular discretisation of the SAAF equation and applied it to a one-dimensional (1D) problem. They also discussed the issues surrounding purely scattering regions as well as voids for the

SAAF equation. The formulation they developed was implemented within a unstructured FE, three-dimensional (3D), neutron transport code called DANTE that has options for both S_N and P_N angular representations [17].

Liscum-Powell et. al. applied the discrete ordinates (S_N) form of the SAAF equation to coupled electron-photon transport and derived a consistent DSA scheme [18]. They utilised a continuous Bubnov-Galerkin spatial discretisation with linear FEs and applied this to one-dimensional (1D) radiation transport problems. Fan et. al. derived an operator form of the SAAF equation angularly discretised using discrete ordinates (S_N) and with anisotropic scattering [19]. Ackroyd developed another variational derivation by considering relaxed forms of the SAAF equation based on trial functions and vectors for the reaction and leakage rates respectively, spatially discretised using FEs [20]. Morel et. al. presented the SAAF, EP, and OP equations applied to general radiative transfer [8]. The self-adjoint angular intensity (SAAI) equation was applied to two-dimensional (2D) problems that were spatially discretised using bi-linear FEs and a discrete ordinate (S_N) angular discretisation. Cao and Wu compared the spherical harmonics (P_N) and discrete ordinate (S_N) angular discretisation methods when applied to the SAAF equation over an unstructured FE mesh [21]. Wang & Gleicher investigated reflective boundary conditions for the SAAF equation proposing a different method that is symmetric but not positive definite [22]. Wang et. al developed a consistent DSA scheme for the SAAF equation that included a void treatment [14]. Schunert et. al. investigated the physical and mathematical adjoint. The reason for this is that the SAAF equation is self-adjoint for the mono-energetic equation but in the multi-group case the scattering and fisson operators are not self-adjoint. The SAAF-S_N equation was spatially discretised using a continuous Bubnov-Galerkin FE discretisation in the radiation transport code Rattle$S_N$ake [23]. Rattle$S_N$ake can use either a discrete ordinate (S_N) or a spherical harmonic (P_N) angular discretisation [24]. The radiation transport code Rattle$S_N$ake is a physics module within the multi-physics code MOOSE [25].

Contemporary unstructured mesh neutron transport calculations are typically spatially discretised using the FE method [25, 26, 27, 28]. In fact most of the unstructured mesh neutron transport literature is devoted to the development of FE based discretisation schemes. However, more recently high-order accurate spectral element (SE) [29, 30, 31, 32] and isogeometric analyis (IGA) methods have been developed for modelling neutron transport [33, 34, 35, 36, 37, 38]. The IGA method is a spatial discretisation methodology first introduced in 2005 by T. J. R Hughes [39]. IGA methods utilise the same NURBS basis function representation as used in CAD geometry software for the test and trial functions within weak forms of a prescribed partial differential equation (PDE). This approach enables the IGA spatial discretisation to provide automatic refinement of the spatial representation whilst preserving the geometry of the domain and without the need for auxiliary mesh generation software. Estimates for the fraction of analysis time spent generating adequate FE meshes are as high as 80% for certain applications [40].

The advantages of IGA compared to the FE method are two-fold. Firstly there is no error due to approximation of geometry, with IGA, both surface area and volume are represented exactly and this is satisfied even on the coarsest mesh. In a nuclear reactor physics context this allows for the exact representation of volume (fissile mass) and surface area (neutron leakage effects) for geometries that can be represented by NURBS [33]. The preservation of volume and surface area are mutually exclusive when using isoparametric tetrahedral or hexahedral meshes for geometries described by NURBS (e.g. conic sections in 2D and quadric surfaces in 3D) [33, 34, 35]. Secondly, the NURBS basis functions used with IGA have high-order continuity over given NURBS patches. Conversely, FE basis functions are at most C^0 continuous between FEs. The higher continuity within a NURBS patch leads to a higher fidelity solution when

representing smooth solutions within a NURBS patch. This is particularly useful when solving elliptic partial differential equations (PDEs) which are often characterised by smooth solutions. For some problems, due to the discontinuous spatial variation in material properties, the solution may exhibit sharp gradients. However, this is usually known ahead of time and the inter-element continuity of the basis functions can be adjusted as will be explained in section 2.

In a neutron transport context, IGA has been applied to the mono-energetic [33] and multi-group [35] neutron diffusion equation, the second-order even-parity equation [34], as well as the first-order neutron transport equation [36, 37, 38]. Throughout all of this work it has been seen that in terms of accuracy per degree of freedom (dof) an IGA spatial discretisation is as least as good as a FE one. Furthermore, the exact representation of geometries has allowed for energy dependent meshing methods to be developed for both first-order [38] and second-order forms of the neutron transport equation [34]. Open-source IGA codes such as GeoPDE's [41] and pyIGA [42] have made the implementation and testing of IGA methods for general PDEs much easier.

In section 2 the basics of IGA and its basis functions are explained. In section 3 the SAAF equation is derived in two ways. Firstly the well known source iteration compatible algebraic derivation from Morel & McGhee's paper [11] is repeated for completeness. Then a novel source iteration compatible variational derivation is performed in a manner similar to Ackroyd's work [16]. This derivation gives a theoretical grounding to the incoming boundary condition used in the algebraic derivation. These two derivations are then shown to be equivalent. Following this section 4 contains details of the IGA spatial and S_N angular discretisations applied to the SAAF equation. Finally numerical results are given in section 5.

2. An introduction to isogeometric analysis (IGA)

IGA is an exact geometry spatial discretisation methodology for geometries that are represented using NURBS basis functions (e.g conic sections in 2D and quadric surfaces in 3D). The NURBS basis functions, used by commercial CAD software to produce geometric models, are used as test and trial functions for the unknown numerical solution allowing for any CAD model to be represented exactly without a mesh having to be generated. Traditionally standard NURBS basis functions are used for this purpose. However, all that is required of the basis functions is their ability to represent CAD geometries exactly. Therefore, different basis functions such as T-splines [43] and hierarchical B-splines [44] can also be used. In this paper we consider only NURBS as there exists computationally efficient methodologies for the evaluation [45] and refinement [46] of NURBS, and assembly of matrices formed from NURBS basis functions [47].

Another important property of NURBS basis functions is their high-order continuity over element boundaries within a NURBS patch, referred to as inter-element continuity. FE basis functions are typically C^0 between elements but NURBS allow arbitrary continuity to be achieved over element boundaries within a NURBS patch. This property has been shown to provide more accuracy per degree of freedom [35] and it allows for more accurate eigen-mode analysis [48]. The effect of these two properties, high-order inter-element continuity and exact geometry representation, on numerical accuracy will be investigated in section 5. The NURBS basis functions, along with the mathematics and algorithms needed to discretise a prescribed partial differential equation (PDE) with the IGA method will now be presented.

2.1. A description of B-spline basis functions

B-splines (basis splines) are piecewise polynomials defined as follows: given a sequence of non-decreasing real numbers - the knot vector $\Xi = \{\xi_1, \xi_2, \ldots, \xi_{m-1}, \xi_m\}$ - and a degree p, the

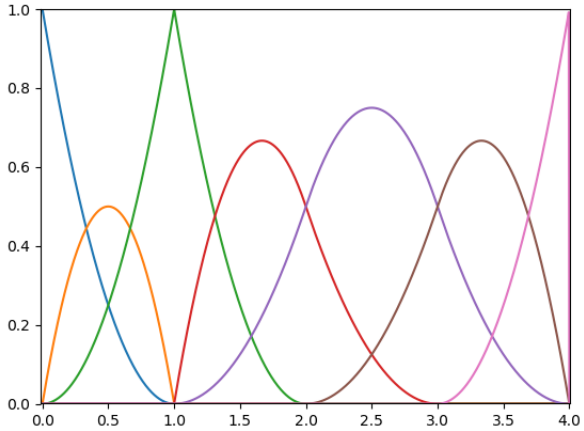

Figure 1: B-spline basis for knot vector $\Xi = (0, 0, 0, 1, 1, 2, 3, 4, 4, 4)$

B-spline basis functions are generated as such:

$$N_{i,0}(\xi) = \begin{cases} 1, & \text{for } \xi \in [\xi_i, \xi_{i+1}) \\ 0, & \text{otherwise} \end{cases}$$

$$N_{i,p}(\xi) = \frac{\xi - \xi_i}{\xi_{i+p} - \xi_i} N_{i,p-1}(\xi) + \frac{\xi_{i+p+1} - \xi}{\xi_{i+p+1} - \xi_{i+1}} N_{i+1,p-1}(\xi), \tag{1}$$

where if the expression $\frac{0}{0}$ occurs that term is assumed to be 0.

In Ξ the i^{th} knot ξ_i can be repeated. This has the effect of reducing the continuity of the B-spline functions over that knot to C^{p-m_i}. m_i is referred to as the multiplicity of the knot and is the number of times the knot appears in Ξ. If a knot only appears once in Ξ, then the basis is C^{p-1} there. For all other $\xi \in [\xi_1, \xi_m]$, $\xi \neq \{\xi_i\}_{i=1}^m$ the B-spline functions are C^∞. This, combined with the fact that the B-splines over Ξ are linearly independent, means that the B-splines defined over Ξ are a basis for the vector space of all piecewise polynomial functions of degree p that are C^{s_i} continuous at $\xi = \xi_i$ for $i \in [1, m]$ with $s_i \in [-1, p)$ [45].

Previous IGA research has concluded that open knot vectors offer several advantages. An open knot vector has the multiplicity of the first and last knots set to $p + 1$. Using these vectors allows for simple implementation of strong Dirichlet boundary conditions, makes the design and manipulation of CAD geometries intuitive, and causes the B-splines to form a partition of unity over Ξ [49]. The partition of unity leads to the strong convex hull property which simplifies certain algorithms further [45]. Open knot vectors are the de facto standard for IGA [40], and we adopt open knot vectors for the entirety of our study. For quadratic B-splines ($p = 2$) an open knot vector could be: $\Xi = \{\xi_1, \xi_1, \xi_1, \xi_2, \xi_3, \xi_4, \xi_4, \xi_4\}$. An example of a B-spline basis or order $p = 2$ formed over an open knot vector with reduced continuity over certain knots is shown in figure 1.

2.2. A description of non-uniform rational B-spline (NURBS) basis functions

NURBS are a generalisation of B-splines that in addition to Ξ require a set of weights $\{w_i\}_{i=1}^N \in \mathbb{R}$, where N is the number of basis functions. For an open knot vector Ξ, $N = m-(p + 1)$

where m is the length of Ξ. The NURBS functions, defined as:

$$R_{i,p}(\xi) = \frac{N_{i,p}(\xi)w_i}{\sum_{j=1}^{N} N_{j,p}(\xi)w_j}, \text{ for } i = 1, 2, \ldots, N, \tag{2}$$

can be shown to form a vector space of piecewise rational polynomials. It is standard to require that the $w_i > 0$ as this leads to the NURBS functions inheriting some of the properties of B-splines such as non-negativity, partition of unity, interpolatory end functions, local support, and the strong convex hull property [45]. Due to the partition of unity formed by the B-spline basis it can be seen that the B-splines are a subset of NURBS when $w_i = 1, \forall i$. Since B-splines are a proper subset of NURBS basis functions, only NURBS will be discussed from now on.

2.2.1. NURBS curves, surfaces, & volumes

Once the one-dimensional basis functions have been generated using expression (2) then choosing a set of control points $\{\mathbf{B}_i\}_{i=1}^{N} \in \mathbb{R}^3$ allows a NURBS curve to be defined as follows:

$$\mathbf{C}(\xi) = \sum_{i=1}^{N} R_{i,p}(\xi)\mathbf{B}_i. \tag{3}$$

Two spaces are then defined, the parametric domain $\hat{V} = [\xi_1, \xi_m]$ and the physical domain, $V = \mathbf{C}(\xi)$ for $\xi \in [\xi_1, \xi_m]$. Furthermore the geometry map $\mathbf{C} : \xi \longmapsto \mathbf{C}(\xi) : \hat{V} \to V$ can be defined. A NURBS curve inherits its properties from the NURBS basis functions used to define it in equation (3) such as, the order p, piecewise polynomial nature, affine invariance, and strong convex hull property. Additionally, because Ξ is an open knot vector the endpoints of the curve are interpolatory at $\mathbf{B}_1$ and $\mathbf{B}_N$, that is $\mathbf{C}(\xi_1) = \mathbf{B}_1$ and $\mathbf{C}(\xi_m) = \mathbf{B}_N$ [45]. This property becomes useful when the concept of patches is introduced.

NURBS surfaces are formed using a simple tensor product structure. Open knot vectors Ξ_ξ and Ξ_η are defined for each dimension and equation (2) is extended in the following way:

$$R^p_{i,j}(\xi, \eta) = \frac{N^p_i(\xi)N^p_j(\eta)w_{i,j}}{\sum_{l=1}^{M}\sum_{k=1}^{N} N^p_k(\xi)N^p_l(\eta)w_{l,k}}, \text{ for } i = 1, \ldots, N \text{ and } j = 1, \ldots M. \tag{4}$$

By defining a new dummy variable the tensor product basis can be rewritten using one index $q \in [1, NM]$. Specification of the surface in $\mathbb{R}^3$ is then done by choosing $\{\mathbf{B}_q\}_{q=1}^{NM}$ and the surface map is given by:

$$\mathbf{S}(\xi, \eta) = \sum_{q=1}^{NM} R_q(\xi, \eta)\mathbf{B}_q, \tag{5}$$

with R_q defined as in (4) with the degree p omitted. This process can be extended to three dimensions with the specification of another open knot vector Ξ_ζ. The usage of open knot vectors, combined with the tensor product procedure means that the bounding $d-1$-dimensional 'surfaces' of a d-dimensional NURBS object are themselves NURBS objects.

NURBS functions can be viewed as B-splines in a four-dimensional homogeneous coordinate system with the weight as the fourth dimension. Because of the division by the weight in expressions (2) and (4) the added generalisation of NURBS functions allows us to represent more complex curves and surfaces. In particular, NURBS functions are able to exactly represent

conic sections in two dimensions and quadric surfaces in three dimensions [40], which is particularly useful for geometries that occur in nuclear engineering. Standard higher-order Lagrangian FE cannot represent conic sections in two dimensions or quadric surfaces in three dimensions exactly as they are not rational polynomial functions [40].

One issue with the tensor product nature of the higher dimensional NURBS objects is that they are always topologically equivalent to a hypercube. Other basis functions, such as T-splines, do not have this problem [43]. However, in this paper only NURBS are investigated. In order to represent complex geometries that differ topologically from a hypercube with NURBS objects, the concept of a patch is introduced.

2.2.2. NURBS patches

A NURBS patch is defined as a grouping of knot vectors, weights, control points, and material coefficients. A collection of NURBS patches allows for the representation of multiply connected domains or domains that are not topologically equivalent to a hypercube. The partitioning of the physical domain into patches also allows for sub-domains of different material properties to be kept distinct. Due to the fact that patch matrices can be assembled independently and h, p, and k refinement can be performed independently on each patch, it forms a convenient way in which to partition the computational load when parallelising code [40].

B-splines and NURBS of degree p exhibit the same theoretical orders of convergence as FE basis functions of the same order. However, as mentioned earlier, it has been seen that splines of maximal smoothness (C^{p-1}) require fewer dof in order to reproduce the same error for neutron diffusion theory [35] and that FE methods require fissile mass preservation techniques in order to match IGA in the case of first-order neutron transport [36]. The increased smoothness and support of spline basis functions leads to complications in other areas: direct solver performance [50], multi-grid methods [51], and domain decomposition algorithms [52] have all required extra study. In this paper the spatial error of the IGA solution is of primary concern.

3. Algebraic derivation of the SAAF neutron transport equation and its associated weak and variational forms

The steady-state (time-independent), first-order, energy-dependent, neutron transport equation is given by [53]:

$$\mathbf{\Omega} \cdot \nabla \psi_o(\mathbf{r}, \mathbf{\Omega}, E) + \sigma_t(\mathbf{r}, E)\psi_o(\mathbf{r}, \mathbf{\Omega}, E) = Q(\mathbf{r}, \mathbf{\Omega}, E), \tag{6}$$

where

$$Q(\mathbf{r}, \mathbf{\Omega}, E) = Q_{\text{scatter}}(\mathbf{r}, \mathbf{\Omega}, E) + Q_{\text{ext}}(\mathbf{r}, E), \tag{7}$$

and

$$Q_{\text{scatter}}(\mathbf{r}, \mathbf{\Omega}, E) = \int_0^\infty \int_{4\pi} \sigma_s(\mathbf{r}, \mathbf{\Omega}' \rightarrow \mathbf{\Omega}, E' \rightarrow E)\psi_o(\mathbf{r}, \mathbf{\Omega}', E')\, d\mathbf{\Omega}' dE'$$

is the source of neutrons due to scatter into energy E, $\psi_o(\mathbf{r}, \mathbf{\Omega}, E)$ is the angular neutron flux $\sigma_t(\mathbf{r}, E)$ is the total macroscopic neutron cross-section, $\sigma_s(\mathbf{r}, \mathbf{\Omega}' \rightarrow \mathbf{\Omega}, E' \rightarrow E)$ is the differential scattering macroscopic neutron cross-section, and $Q_{\text{ext}}(\mathbf{r}, E)$ is a source composed of fission sources and fixed (extraneous) sources.

The vacuum and incoming surface source conditions are assumed to be prescribed for the incoming boundary condition:

$$\psi_o(\mathbf{r}, \mathbf{\Omega}, E) = 0 \quad \text{for } \mathbf{\Omega} \cdot \mathbf{n} < 0 \text{ and } \mathbf{r} \in S_b, \tag{8}$$

$$\psi_o(\mathbf{r}, \mathbf{\Omega}, E) = T(\mathbf{r}, \mathbf{\Omega}, E) \quad \text{for } \mathbf{\Omega} \cdot \mathbf{n} < 0 \text{ and } \mathbf{r} \in S_s, \tag{9}$$

where $S_b \cup S_s = S$ forms the boundary of the computational domain. It should be noted that a reflective boundary condition is a special case of an incoming source with

$$T(\mathbf{r}, \mathbf{\Omega}, E) = \psi_o(\mathbf{r}, \mathbf{\Omega}', E) \quad \text{for } \mathbf{r} \in S_r \text{ and } \mathbf{\Omega} \cdot \mathbf{n} < 0,$$

where $\mathbf{\Omega}'$ is the angle of specular reflection for $\mathbf{\Omega}$. Together these three boundary conditions highlight the general form of the boundary conditions used in neutron transport theory [26].

What follows are two derivations of the second-order SAAF equation. Firstly an algebraic source iteration compatible derivation taken from work by Morel & Mcghee [11] and secondly a maximum variational principle is derived that is shown to yield the source iteration compatible SAAF equation along with natural boundary conditions for the incoming and outgoing angles.

3.1. Algebraic derivation of the SAAF form of the neutron transport equation

Rearranging equation (6) for the angular flux gives:

$$\psi_o(\mathbf{r}, \mathbf{\Omega}, E) = \frac{1}{\sigma_t(\mathbf{r}, E)} \left[Q(\mathbf{r}, \mathbf{\Omega}, E) - \mathbf{\Omega} \cdot \nabla \psi_o(\mathbf{r}, \mathbf{\Omega}, E) \right], \tag{10}$$

which is then substituted back into the first term of the first-order neutron transport equation yielding:

$$-\mathbf{\Omega} \cdot \nabla \frac{1}{\sigma_t(\mathbf{r}, E)} \mathbf{\Omega} \cdot \nabla \psi_o(\mathbf{r}, \mathbf{\Omega}, E) + \sigma_t(\mathbf{r}, E) \psi_o(\mathbf{r}, \mathbf{\Omega}, E) = Q(\mathbf{r}, \mathbf{\Omega}, E) - \left(\mathbf{\Omega} \cdot \nabla \frac{Q(\mathbf{r}, \mathbf{\Omega}, E)}{\sigma_t(\mathbf{r}, E)} \right). \tag{11}$$

Implicit in the rearrangement step is the requirement that $\sigma_t \neq 0$. This means that in the above form the SAAF equation is not compatible with voided regions. As is noted by Morel & McGhee [11], this formulation of the SAAF equation is suitable for source iteration due to the fact that the operator on the left hand side is self-adjoint in the energy dependent case. This also obviates any issues singularities in regions of pure scattering as there is no $(\sigma_t - \sigma_s)$ term in the denominator as is possible in certain forms of the SAAF equation.

The incoming boundary conditions for SAAF can also be derived algebraically from the first-order boundary conditions:

$$\psi_o(\mathbf{r}, \mathbf{\Omega}, E) = \frac{1}{\sigma_t(\mathbf{r}, E)} \left(Q(\mathbf{r}, \mathbf{\Omega}, E) - \mathbf{\Omega} \cdot \nabla \psi_o(\mathbf{r}, \mathbf{\Omega}, E) \right) = T(\mathbf{r}, \mathbf{\Omega}, E) \quad \text{for } \mathbf{r} \in S_s \tag{12}$$

$$\psi_o(\mathbf{r}, \mathbf{\Omega}, E) = \frac{1}{\sigma_t(\mathbf{r}, E)} \left(Q(\mathbf{r}, \mathbf{\Omega}, E) - \mathbf{\Omega} \cdot \nabla \psi_o(\mathbf{r}, \mathbf{\Omega}, E) \right) = 0 \quad \text{for } \mathbf{r} \in S_b. \tag{13}$$

In addition, due to SAAF being second-order, extra boundary conditions for the outgoing flux must be prescribed. Morel & McGhee [11] suggest that the outgoing flux on the boundary should satisfy the first-order neutron transport equation, that is:

$$\psi_o(\mathbf{r}, \mathbf{\Omega}, E) = \frac{1}{\sigma_t(\mathbf{r}, E)} \left(Q(\mathbf{r}, \mathbf{\Omega}, E) - \mathbf{\Omega} \cdot \nabla \psi_o(\mathbf{r}, \mathbf{\Omega}, E) \right) \quad \text{for } \mathbf{r} \in S \tag{14}$$

claiming that it is "a natural way to ensure that spurious solutions to the SAAF equation are eliminated." It will be seen in the next section that this boundary condition can be derived from a maximum variational principle.

3.1.1. The weak form of the SAAF neutron transport equation

Equation (11) is the strong form of the SAAF equation. It is assumed that an approximation to ψ_o must be found. In order to form a system of linear equations that represent equation (11) and allow the computation of an approximate solution, a weak form must be generated by using a weighted residual (WR) method.

We consider a weighting function $w(\mathbf{r})$ from the space of admissible functions. A function u is an admissible function if u and $\mathbf{\Omega} \cdot \nabla u$ are continuous functions of $\mathbf{r}$ and $\mathbf{\Omega}$ almost everywhere within a given patch [54]. No assumptions are made about the boundary conditions that an admissible function must satisfy.

The strong form equation is multiplied by a weighting function and integration is performed over the entire spatial domain:

$$\begin{aligned}\int_V \Big[w(\mathbf{r})\mathbf{\Omega} \cdot \nabla \frac{1}{\sigma_t(\mathbf{r}, E)} \Big(-\mathbf{\Omega} \cdot \nabla \psi_o(\mathbf{r}, \mathbf{\Omega}, E) + Q(\mathbf{r}, \mathbf{\Omega}, E) \Big) \\ w(\mathbf{r}) \Big(\sigma_t(\mathbf{r}, E) \psi_o(\mathbf{r}, \mathbf{\Omega}, E) - Q(\mathbf{r}, \mathbf{\Omega}, E) \Big) \Big] d\mathbf{r} = 0.\end{aligned} \tag{15}$$

Suppressing explicit dependencies for brevity and applying Green's first identity to the first term in the spatial integral yields:

$$\int_V \left[\left(\frac{\mathbf{\Omega} \cdot \nabla w}{\sigma_t} \right) (\mathbf{\Omega} \cdot \nabla \psi_o - Q) + w \left(\sigma_t \psi_o - Q \right) \right] d\mathbf{r} + \int_S (\mathbf{\Omega} \cdot \mathbf{n}) \frac{w}{\sigma_t} \left(-\mathbf{\Omega} \cdot \nabla \psi_o + Q \right) d\mathbf{r}_s = 0 \tag{16}$$

where $\mathbf{r}_s$ refers to points on surface S. The above equation is the weak form of the SAAF equation and the weighting (test) function can be chosen in order to form either a Bubnov-Galerkin or Petrov-Galerkin discretisation of the weak form.

3.2. Source iteration compatible variational formulation of the SAAF neutron transport equation

This variational derivation is based on work done by Ackroyd in two papers [16, 54] and the following notation is adopted:

$$\langle u, v \rangle = \int_{4\pi} uv \, d\mathbf{\Omega}. \tag{17}$$

It is also noted that:

$$\int_{4\pi} (\mathbf{\Omega} \cdot \mathbf{n}) f(\mathbf{\Omega}) \, d\mathbf{\Omega} = \int_{\mathbf{\Omega} \cdot \mathbf{n} > 0} |\mathbf{\Omega} \cdot \mathbf{n}| f(\mathbf{\Omega}) \, d\mathbf{\Omega} - \int_{\mathbf{\Omega} \cdot \mathbf{n} < 0} |\mathbf{\Omega} \cdot \mathbf{n}| f(\mathbf{\Omega}) \, d\mathbf{\Omega}. \tag{18}$$

where $f(\mathbf{\Omega})$ is some function that depends on the solid angle $\mathbf{\Omega}$.

In the original derivation by Ackroyd the following operator is defined:

$$\Sigma f(\mathbf{r}, \mathbf{\Omega}) = \sigma_t(\mathbf{r}) f(\mathbf{r}, \mathbf{\Omega}) - \int_{4\pi} \sigma_s(\mathbf{r}, \mathbf{\Omega}' \cdot \mathbf{\Omega}) f(\mathbf{r}, \mathbf{\Omega}') \, d\mathbf{\Omega}'. \tag{19}$$

and it can be shown that

1. Σ has an inverse,
2. Σ and Σ^{-1} are self-adjoint,
3. Σ and Σ^{-1} are positive definite.

These results are proven in Appendix A of Ackroyd's work [16].

In this derivation, in order to ensure that the variational problem will be compatible with source iteration the scattering kernel is considered as part of the source and a new choice of Σ is made:

$$\Sigma(\mathbf{r})f(\mathbf{r},\mathbf{\Omega}) = \sigma_t(\mathbf{r})f(\mathbf{r},\mathbf{\Omega}). \tag{20}$$

This choice of Σ clearly satisfies the conditions laid out above with the inverse:

$$\Sigma^{-1}(\mathbf{r}) = \frac{1}{\sigma_t(\mathbf{r})},$$

except where $\sigma_t \neq 0$ as then the inverse is not defined.

Then the following functional is defined:

$$F(u,v) = \int_V \left[\left\langle \mathbf{\Omega}\cdot\nabla u, \Sigma^{-1}\mathbf{\Omega}\cdot\nabla v\right\rangle + \langle u, \Sigma v\rangle\right] d\mathbf{r} + \int_S\int_\Omega |\mathbf{\Omega}\cdot\mathbf{n}| uv d\mathbf{\Omega} dS \tag{21}$$

where u, v are admissible functions and the list of dependent variables has been omitted for brevity. The choice of $F(u,v)$ is based on the following observations:

1. Σ^{-1} operates on $\mathbf{\Omega}\cdot\nabla\psi_o$ in equation (11),
2. Σ operates on ψ_o in equation (11),
3. All terms in $F(u,u)$ are strictly positive for all u (except at $u = 0$ where $F(0,0) = 0$) as Σ and Σ^{-1} are positive definite.

It is noted that:

$$F(u,\psi_o) = \int_V \left[\left\langle \mathbf{\Omega}\cdot\nabla u, \Sigma^{-1}\mathbf{\Omega}\cdot\nabla\psi_o\right\rangle + \langle u, \Sigma\psi_o\rangle\right] d\mathbf{r} + \int_S\int_\Omega |\mathbf{\Omega}\cdot\mathbf{n}| u\psi_o \, d\mathbf{\Omega}\, dS, \tag{22}$$

where ψ_o is the exact solution of equation (6). The volume integral in equation (22) can be simplified giving:

$$\begin{aligned}
&\int_V \left[\left\langle \mathbf{\Omega}\cdot\nabla u, \Sigma^{-1}\mathbf{\Omega}\cdot\nabla\psi_o\right\rangle + \langle u, \Sigma\psi_o\rangle\right] d\mathbf{r} \\
&= \int_V \left[\left\langle \mathbf{\Omega}\cdot\nabla u, \Sigma^{-1}Q - \psi_o\right\rangle + \langle u, Q - \mathbf{\Omega}\cdot\nabla\psi_o\rangle\right] d\mathbf{r} \\
&= \int_V \left[\left\langle \mathbf{\Omega}\cdot\nabla u, \Sigma^{-1}Q\right\rangle - \langle \mathbf{\Omega}\cdot\nabla u, \psi_o\rangle + \langle u, Q\rangle - \langle u, \mathbf{\Omega}\cdot\nabla\psi_o\rangle\right] d\mathbf{r}.
\end{aligned}$$

The identity $\mathbf{\Omega}\cdot\nabla(u\psi_o) = (\mathbf{\Omega}\cdot\nabla u)\psi_o + u(\mathbf{\Omega}\cdot\nabla\psi_o)$ along with the divergence theorem is used:

$$\begin{aligned}
&\int_V \left[\left\langle \mathbf{\Omega}\cdot\nabla u, \Sigma^{-1}Q\right\rangle + \langle u, Q\rangle\right] d\mathbf{r} - \int_V\int_\Omega \mathbf{\Omega}\cdot\nabla(u\psi_o)\, d\mathbf{\Omega}\, d\mathbf{r} \\
&= \int_V \left[\left\langle \mathbf{\Omega}\cdot\nabla u, \Sigma^{-1}Q\right\rangle + \langle u, Q\rangle\right] d\mathbf{r} - \int_S\int_\Omega (\mathbf{\Omega}\cdot\mathbf{n}) u\psi_o \, d\mathbf{\Omega}\, dS \\
&= \int_V \left[\left\langle \mathbf{\Omega}\cdot\nabla u, \Sigma^{-1}Q\right\rangle + \langle u, Q\rangle\right] \mathbf{r} - \int_S\int_{\mathbf{\Omega}\cdot\mathbf{n}>0} |\mathbf{\Omega}\cdot\mathbf{n}| u\psi_o \, d\mathbf{\Omega}\, dS + \int_S\int_{\mathbf{\Omega}\cdot\mathbf{n}<0} |\mathbf{\Omega}\cdot\mathbf{n}| u\psi_o \, d\mathbf{\Omega}\, dS.
\end{aligned}$$

where the integral over angle has been split into two half range integrals according to equation (18). Therefore, we have that

$$F(u,\psi_o) = \int_V \left[\left\langle \mathbf{\Omega}\cdot\nabla u, \Sigma^{-1}Q\right\rangle + \langle u, Q\rangle\right] d\mathbf{r} + 2\int_S\int_{\mathbf{\Omega}\cdot\mathbf{n}<0} |\mathbf{\Omega}\cdot\mathbf{n}| u\psi_o \, d\mathbf{\Omega}\, dS \tag{23}$$

is independent of ψ_o once boundary conditions have been prescribed. Here the boundary conditions, given by equations (12) & (13), for ψ_o can be prescribed yielding the following expression:

$$F(u,\psi_o) = \int_V \left[\left\langle \mathbf{\Omega}\cdot\nabla u, \Sigma^{-1}Q\right\rangle + \langle u, Q\rangle\right] d\mathbf{r} + 2\int_{S_s}\int_{\mathbf{\Omega}\cdot\mathbf{n}<0} |\mathbf{\Omega}\cdot\mathbf{n}| uT\, d\mathbf{\Omega}\, dS. \tag{24}$$

An admissible function ϕ is considered where ϕ is a variation from the exact solution ψ_o. Applying F to the error gives:

$$F(\psi_o - \lambda\phi, \psi_o - \lambda\phi) = F(\psi_o,\psi_o) - 2\lambda(\phi,\psi_o) + \lambda^2 F(\phi,\phi) \geq 0, \tag{25}$$

which implies

$$2\lambda F(\phi,\psi_o) - \lambda^2 F(\phi,\phi) \leq F(\psi_o,\psi_o). \tag{26}$$

This provides a mechanism for generating maximum principles for the neutron transport equation, depending on λ, as equality of equation (26) is only seen when $(\psi_o - \lambda\phi) \to 0$. Here $\lambda = 1$ is chosen and the maximum principle $K(\phi) = 2F(\phi,\psi_o) - F(\phi,\phi)$ is defined where:

$$\begin{aligned} K(\phi) = &\int_V \left[2\langle\phi, Q\rangle + 2\left\langle \mathbf{\Omega}\cdot\nabla\phi, \Sigma^{-1}Q\right\rangle - \left\langle \mathbf{\Omega}\cdot\nabla\phi, \Sigma^{-1}\mathbf{\Omega}\cdot\nabla\phi\right\rangle - \langle\phi,\Sigma\phi\rangle\right] d\mathbf{r} \\ &+4\int_{S_s}\int_{\mathbf{\Omega}\cdot\mathbf{n}<0} |\mathbf{\Omega}\cdot\mathbf{n}|\phi T\, d\mathbf{\Omega} dS - \int_S\int_\Omega |\mathbf{\Omega}\cdot\mathbf{n}|\phi^2 dS \end{aligned} \tag{27}$$

and $K(\phi)$ is independent of the exact solution ψ_o.

In order to find extrema the first variation of $K(\phi)$ must be considered, in particular where it is stationary. A variation of the exact solution is considered $\phi = \psi_o + \epsilon\xi$ and $K(\psi_o + \epsilon\xi)$ is evaluated:

$$\begin{aligned} K(\psi_o+\epsilon\xi) \equiv I(\epsilon) = &\int_V \left[2\langle\psi_o+\epsilon\xi, Q\rangle + 2\left\langle \mathbf{\Omega}\cdot\nabla(\psi_o+\epsilon\xi), \Sigma^{-1}Q\right\rangle\right. \\ &\left. - \left\langle \mathbf{\Omega}\cdot\nabla(\psi_o+\epsilon\xi), \Sigma^{-1}\mathbf{\Omega}\cdot\nabla(\psi_o+\epsilon\xi)\right\rangle - \langle(\psi_o+\epsilon\xi), \Sigma(\psi_o+\epsilon\xi)\rangle\right] d\mathbf{r} \\ &+4\int_{S_s}\int_{\mathbf{\Omega}\cdot\mathbf{n}<0} |\mathbf{\Omega}\cdot\mathbf{n}|(\psi_o+\epsilon\xi) T\, d\mathbf{\Omega}\, dS - \int_S\int_\Omega |\mathbf{\Omega}\cdot\mathbf{n}|(\psi_o+\epsilon\xi)^2\, d\mathbf{\Omega}\, dS. \end{aligned} \tag{28}$$

To find stationary points the following equality is considered

$$\left(\frac{dI(\epsilon)}{d\epsilon}\right)_{\epsilon=0} = 0, \tag{29}$$

giving

$$\begin{aligned} 0 = \int_V\Big[\int_\Omega \Big(&2\xi Q + 2\mathbf{\Omega}\cdot\nabla\xi(\Sigma^{-1}Q) - (\mathbf{\Omega}\cdot\nabla\psi_o)(\Sigma^{-1}\mathbf{\Omega}\cdot\nabla\xi) - (\mathbf{\Omega}\cdot\nabla\xi)(\Sigma^{-1}\mathbf{\Omega}\cdot\nabla\psi_o) \\ &-\psi_o\Sigma\xi - \xi\Sigma\psi_o\Big) d\mathbf{\Omega}\Big] d\mathbf{r} + 4\int_{S_s}\int_{\mathbf{\Omega}\cdot\mathbf{n}<0} |\mathbf{\Omega}\cdot\mathbf{n}|\xi T\, d\mathbf{\Omega}\, dS - 2\int_S\int_\Omega |\mathbf{\Omega}\cdot\mathbf{n}|\psi_o\xi\, d\mathbf{\Omega}\, dS. \end{aligned} \tag{30}$$

The volume integral terms can be simplified:

$$\begin{aligned} &2\int_V\left[\int_\Omega \left(\xi Q + \mathbf{\Omega}\cdot\nabla\xi(\Sigma^{-1}Q) - (\mathbf{\Omega}\cdot\nabla\xi)(\Sigma^{-1}\mathbf{\Omega}\cdot\nabla\psi_o) - \xi\Sigma\psi_o\right) d\mathbf{\Omega}\right] d\mathbf{r} \\ &= 2\int_V\int_\Omega (Q - \Sigma\psi_o)\xi + \left[\Sigma^{-1}(Q - \mathbf{\Omega}\cdot\nabla\psi_o)\right](\mathbf{\Omega}\cdot\nabla\xi)\, d\mathbf{\Omega}\, d\mathbf{r}, \end{aligned}$$

with the chain rule and the divergence theorem being used on the second term:

$$\begin{aligned}
&\int_V \Sigma^{-1}(Q - \mathbf{\Omega}\cdot\nabla\psi_o)(\mathbf{\Omega}\cdot\nabla\xi)\,d\mathbf{r} \\
&= \int_V \left[\nabla\cdot\left(\mathbf{\Omega}\xi\Sigma^{-1}\left(Q - \mathbf{\Omega}\cdot\nabla\psi_o\right)\right) - \xi\mathbf{\Omega}\cdot\nabla\Sigma^{-1}\left(Q - \mathbf{\Omega}\cdot\nabla\psi_o\right)\right] d\mathbf{r} \\
&= \int_S \int_\Omega \mathbf{\Omega}\cdot\mathbf{n}\xi\Sigma^{-1}\left(Q - \mathbf{\Omega}\cdot\nabla\psi_o\right)\,d\mathbf{\Omega}\,dS - \int_V \xi\mathbf{\Omega}\cdot\nabla\Sigma^{-1}\left(Q - \mathbf{\Omega}\cdot\nabla\psi_o\right)\,d\mathbf{r}.
\end{aligned}$$

The surface integral can be written as:

$$\begin{aligned}
&4\int_{S_s}\int_\Omega |\mathbf{\Omega}\cdot\mathbf{n}|\xi T\,d\mathbf{\Omega}\,dS - 2\int_S\int_\Omega |\mathbf{\Omega}\cdot\mathbf{n}|\psi_o\xi\,d\mathbf{\Omega}\,dS \\
=&2\int_{S_s}\int_\Omega |\mathbf{\Omega}\cdot\mathbf{n}|\xi(2T - \psi_o)\,d\mathbf{\Omega}\,dS - 2\int_{S_b}\int_\Omega |\mathbf{\Omega}\cdot\mathbf{n}|\xi\psi_o\,d\mathbf{\Omega}\,dS,
\end{aligned}$$

where the range of the angular integral over S_S has been increased to all of $\mathbf{\Omega}$ by noting that $T(\mathbf{\Omega}) = 0$ for $\mathbf{\Omega}\cdot\mathbf{n} > 0$. Recombining the volume and surface terms yields:

$$\begin{aligned}
0 = &\int_V\int_\Omega \xi\left[Q - \Sigma\psi_o - \mathbf{\Omega}\cdot\nabla\Sigma^{-1}\left(Q - \mathbf{\Omega}\cdot\nabla\psi_o\right)\right] d\mathbf{\Omega}\,d\mathbf{r} + \int_{S_S}\int_\Omega \xi\left[|\mathbf{\Omega}\cdot\mathbf{n}|(2T - \psi_o)\right. \\
&\left. + \mathbf{\Omega}\cdot\mathbf{n}\Sigma^{-1}\left(Q - \mathbf{\Omega}\cdot\nabla\psi_o\right)\right] d\mathbf{\Omega}\,dS - \int_{S_b}\int_\Omega \xi\left[|\mathbf{\Omega}\cdot\mathbf{n}|\psi_o - \mathbf{\Omega}\cdot\mathbf{n}\Sigma^{-1}\left(Q - \mathbf{\Omega}\cdot\nabla\psi_o\right)\right] d\mathbf{\Omega}\,dS,
\end{aligned}$$

and applying the fundamental lemma of the calculus of variations yields:

$$\begin{aligned}
0 = &\int_V\int_\Omega \left[Q - \Sigma\psi_o - \mathbf{\Omega}\cdot\nabla\Sigma^{-1}\left(Q - \mathbf{\Omega}\cdot\nabla\psi_o\right)\right] d\mathbf{\Omega}\,d\mathbf{r} + \int_{S_S}\int_\Omega \left[|\mathbf{\Omega}\cdot\mathbf{n}|(2T - \psi_o)\right. \\
&\left. + \mathbf{\Omega}\cdot\mathbf{n}\Sigma^{-1}\left(Q - \mathbf{\Omega}\cdot\nabla\psi_o\right)\right] d\mathbf{\Omega}\,dS - \int_{S_b}\int_\Omega \left[|\mathbf{\Omega}\cdot\mathbf{n}|\psi_o - \mathbf{\Omega}\cdot\mathbf{n}\Sigma^{-1}\left(Q - \mathbf{\Omega}\cdot\nabla\psi_o\right)\right] d\mathbf{\Omega}\,dS.
\end{aligned} \tag{31}$$

The SAAF equation along with its boundary conditions can be recovered yielding the following equations:

$$-\mathbf{\Omega}\cdot\nabla(\Sigma^{-1}\mathbf{\Omega}\cdot\nabla\psi_o) + \Sigma\psi_o = Q - \mathbf{\Omega}\cdot\nabla\Sigma^{-1}Q \tag{32}$$

$$|\mathbf{\Omega}\cdot\mathbf{n}|(2T - \psi_o) + \mathbf{\Omega}\cdot\mathbf{n}\Sigma^{-1}(Q - \mathbf{\Omega}\cdot\nabla\psi_o) = 0 \quad \text{on } S_s \tag{33}$$

$$|\mathbf{\Omega}\cdot\mathbf{n}|\psi_o - \mathbf{\Omega}\cdot\mathbf{n}\Sigma^{-1}(Q - \mathbf{\Omega}\cdot\nabla\psi_o) = 0 \quad \text{on } S_b \tag{34}$$

in particular, the boundary conditions can decomposed into expressions for incoming and outgoing directions to the boundary as follows:
$\underline{\mathbf{\Omega}\cdot\mathbf{n} < 0}$:

$$2T - \psi_o - \Sigma^{-1}\left(Q - \mathbf{\Omega}\cdot\nabla\psi_o\right) = 0 \Rightarrow \psi_o = T \quad \text{for } \mathbf{r}\in S_s, \tag{35}$$

$$\psi_o + \Sigma^{-1}\left(Q - \mathbf{\Omega}\cdot\nabla\psi_o\right) = 0 \Rightarrow \psi_o = 0 \quad \text{for } \mathbf{r}\in S_b, \tag{36}$$

$\underline{\mathbf{\Omega}\cdot\mathbf{n} > 0}$:

$$\psi_o - \Sigma^{-1}\left(Q - \mathbf{\Omega}\cdot\nabla\psi_o\right) = 0 \Rightarrow \psi_o = \Sigma^{-1}\left(-\mathbf{\Omega}\cdot\nabla\psi_o + Q\right) \quad \text{for } \mathbf{r}\in S. \tag{37}$$

Not only do the incoming boundary conditions match the boundary conditions for the first-order form of the neutron transport equation, but the outgoing boundary condition postulated by Morel & McGhee is found as a natural consequence of the maximum principle. This variational derivation will not be valid for void regions due to the choice of the operator Σ. In the case of a void the inverse of the operator Σ will be singular. In addition as this variational principle is not valid for void regions the outgoing boundary condition is also not valid for void regions.

3.3. Equivalence of algebraic and variational derivation of the SAAF form of the neutron transport equation

The weak form from the algebraic derivation is given by equation (16). Angular integration is performed over the surface and is split into incoming and outgoing angles according to equation (18):

$$\begin{aligned}
&\int_{4\pi}\int_{V}\left[\left(\frac{\mathbf{\Omega}\cdot\nabla w}{\sigma_t}\right)(\mathbf{\Omega}\cdot\nabla\psi - Q) + w\,(\sigma_t\psi - Q)\right] d\mathbf{r}\,d\mathbf{\Omega} \\
&+\int_{\mathbf{\Omega}\cdot\mathbf{n}>0}\int_{S}\left[|\mathbf{\Omega}\cdot\mathbf{n}|\frac{w}{\sigma_t}\,(-\mathbf{\Omega}\cdot\nabla\psi + Q)\right] d\mathbf{r}_s\,d\mathbf{\Omega} \\
&-\int_{\mathbf{\Omega}\cdot\mathbf{n}<0}\int_{S}|\mathbf{\Omega}\cdot\mathbf{n}|\frac{w}{\sigma_t}\,(-\mathbf{\Omega}\cdot\nabla\psi + Q)\;d\mathbf{r}_s\,d\mathbf{\Omega} = 0.
\end{aligned} \tag{38}$$

From the variational derivation we consider equation (23) substituted into equation (26) without applying the boundary conditions that are given for ψ_o. By following through with the rest of the derivation and considering the zeroing of the first variation (see equation 29) an analogous expression to equation (30) is derived, that is:

$$\begin{aligned}
0 = &\int_{V}\left[\int_{\Omega}\xi Q + \mathbf{\Omega}\cdot\nabla\xi(\Sigma^{-1}Q) - (\mathbf{\Omega}\cdot\nabla\psi_o)(\Sigma^{-1}\mathbf{\Omega}\cdot\nabla\xi) - \xi\Sigma\psi_o\,d\mathbf{\Omega}\right] d\mathbf{r} \\
&+2\int_{S}\int_{\mathbf{\Omega}\cdot\mathbf{n}<0}|\mathbf{\Omega}\cdot\mathbf{n}|\xi\psi_o\,d\mathbf{\Omega}\,dS - \int_{S}\int_{\mathbf{\Omega}}|\mathbf{\Omega}\cdot\mathbf{n}|\psi_o\xi\,d\mathbf{\Omega}\,dS.
\end{aligned} \tag{39}$$

Simplifying the equation and multiplying by -1 we are left with:

$$\begin{aligned}
0 = &\int_{V}\left[\int_{\Omega}(\mathbf{\Omega}\cdot\nabla\xi)\Sigma^{-1}\,(\mathbf{\Omega}\cdot\nabla\psi_o - Q) + \xi\,(\Sigma\psi_o - Q)\,d\mathbf{\Omega}\right] d\mathbf{r} \\
&-\int_{S}\int_{\mathbf{\Omega}\cdot\mathbf{n}<0}|\mathbf{\Omega}\cdot\mathbf{n}|\xi\psi_o\,d\mathbf{\Omega}\,dS + \int_{S}\int_{\mathbf{\Omega}}|\mathbf{\Omega}\cdot\mathbf{n}|\psi_o\xi\,d\mathbf{\Omega}\,dS.
\end{aligned} \tag{40}$$

Using the fact that $\psi_o = \frac{1}{\sigma_t}(-\mathbf{\Omega}\cdot\nabla\psi_o + Q)$, replacing ξ with w, and ψ_0 with ψ it can be seen that the variational principle yields the same weak form as the algebraic derivation as is expected of symmetric operators [55].

4. Spatial and angular discretisation of the weak form of the SAAF neutron transport equation

4.1. Bubnov-Galerkin IGA approximation

Similarly to FE methods the solution is assumed to be a linear combination of trial functions:

$$\psi(\mathbf{r},\mathbf{\Omega},E) = \sum_{i=1}^{\infty} d_i(\mathbf{\Omega},E)v_i(\mathbf{r}), \tag{41}$$

where the $d_i \in \mathbb{R}$ are referred to as the control variables and $v_i \in T_R$ are the trial functions. The infinite dimensional trial function space is defined as:

$$T_R = \left\{ v \mid v \in H^1(V),\ v|_{S_D} = g \right\}. \tag{42}$$

Furthermore, w is taken to be a member of an infinite dimensional test function space:

$$T_E = \left\{ w \mid w \in H^1(V),\ w|_S = 0 \right\}, \tag{43}$$

where $H^1(V)$ is the Sobolev space $W_2^1(V)$ over the domain V [56]. The condition $v|_{S_D} = g$ comes from a Dirichlet boundary condition that may be given for $\psi(\mathbf{r}) = g$ for $\mathbf{r} \in S_D$.

In order to provide closure to equation (41) the expansion must be truncated. To do this finite dimensional analogues of T_R and T_E are defined:

$$T_R^h = \left\{ v_i^h \mid v_i^h \in H^1(V),\ v_i^h|_{S_D} = g,\ \text{for } i \in [1, N] \right\},$$
$$T_E^h = \left\{ w_i^h \mid w_i^h \in H^1(V),\ w_i^h|_S = 0,\ \text{for } i \in [1, N] \right\},$$

and the solution is approximated as:

$$\psi(\mathbf{r}, \mathbf{\Omega}, E) \approx \psi^h(\mathbf{r}, \mathbf{\Omega}, E) = \sum_{i=1}^{N} d_i(\mathbf{\Omega}, E) v_i^h(\mathbf{r}). \tag{44}$$

A Bubnov-Galerkin IGA discretisation is then applied by making the choices $v_i(\mathbf{r}) = R_i^p(\mathbf{r}) \in T_R^h$ and $w_j(\mathbf{r}) = R_j^p(\mathbf{r}) \in T_E^h$. This encapsulates the essence of IGA, to use a basis capable of exactly representing the known geometry as a basis for the fields we wish to approximate [40].

4.2. Angular ($\mathbf{\Omega}$) discretisation of the SAAF neutron transport equation

The method of discrete ordinates (S_N) is chosen to discretise the angular domain. Integration with respect to $\mathbf{\Omega}$ is performed via a summation of functions evaluated at certain angles and scaled by certain weights. These angles and weights are referred to as the quadrature set. For example, the scalar neutron flux ϕ can be calculated from the angular neutron flux ψ in the following way:

$$\phi(\mathbf{r}, E) = \int_{4\pi} \psi(\mathbf{r}, \mathbf{\Omega}, E) d\mathbf{\Omega} \approx \sum_{m=1}^{M} w_m \psi(\mathbf{r}, \mathbf{\Omega}_m, E) = \sum_{m=1}^{M} w_m \psi_m(\mathbf{r}, E). \tag{45}$$

By solving equation (11) over the directions $\{\mathbf{\Omega}_m\}_{m=1}^M$ the scalar flux can be recovered using the above quadrature rule. Therefore, the weak form of the SAAF equation given by equation (16) evaluated at $\{\mathbf{\Omega}_m\}_{m=1}^M$ will be considered:

$$\int_V \left[\left(\frac{\mathbf{\Omega}_m \cdot \nabla w}{\sigma_t} \right) (\mathbf{\Omega}_m \cdot \nabla \psi_m - Q_m) + w (\sigma_t \psi_m - Q_m) \right] d\mathbf{r} + \int_S (\mathbf{\Omega}_m \cdot \mathbf{n}) \frac{w}{\sigma_t} (-\mathbf{\Omega}_m \cdot \nabla \psi_o + Q_m) d\mathbf{r}_s = 0, \quad \text{for } m = 1, \ldots, M. \tag{46}$$

The relevant boundary conditions are found by evaluating (35)-(37) for $\mathbf{\Omega} = \mathbf{\Omega}_m$. The above equation (46) is referred to as the S_N-SAAF equation. As equation (45) is a general quadrature

formula, a quadrature set that can adequately represent the angular integrals must be chosen. In this work level-symmetric and Legendre-Chebyshev quadrature sets are used, in particular triangular ones where the order of the polar quadrature order is set to two. This yields a quadrature set that gives the same number of directions as the level-symmetric set but is not identical.

4.3. IGA spatial discretisation of the weak form of the SAAF neutron transport equation

In order to spatially discretise equation (46), equation (44), the choice $w(\mathbf{r}) = R_j^q(\mathbf{r})$, and the boundary conditions given in equations (35)-(37) are substituted into the angularly discretised weak form given in equation (46). This yields the following equation set depending on the sign of $\mathbf{\Omega}_m \cdot \mathbf{n}$:

$\underline{\mathbf{\Omega}_m \cdot \mathbf{n} < 0}$:

$$\sum_{i=1}^{N} d_{i,m} \int_V \left(\frac{1}{\sigma_t} (\mathbf{\Omega}_m \cdot \nabla R_i^q)(\mathbf{\Omega}_m \cdot \nabla R_j^q) + \sigma_t R_i^q R_j^q \right) d\mathbf{r} = \int_V \left(Q_m R_j^q - \frac{Q_m}{\sigma_t} (\mathbf{\Omega}_m \cdot \nabla R_j^q) \right) d\mathbf{r} - \int_S \left(|\mathbf{\Omega}_m \cdot \mathbf{n}| Z R_j^q \right) d\mathbf{r}_s, \tag{47}$$

$\underline{\mathbf{\Omega}_m \cdot \mathbf{n} > 0}$:

$$\sum_{i=1}^{N} d_{i,m} \left[\int_V \left(\frac{1}{\sigma_t} (\mathbf{\Omega}_m \cdot \nabla R_i^q)(\mathbf{\Omega}_m \cdot \nabla R_j^q) + \sigma_t R_i^q R_j^q \right) d\mathbf{r} - \int_S \left(|\mathbf{\Omega}_m \cdot \mathbf{n}| R_i^q R_j^q \right) d\mathbf{r}_s \right] = \int_V \left(Q_m R_j^q - \frac{Q_m}{\sigma_t} (\mathbf{\Omega}_m \cdot \nabla R_j^q) \right) d\mathbf{r}, \quad \text{for } m = 1, \ldots, M \tag{48}$$

where q is the order of the NURBS basis functions, $Z(\mathbf{r}, \mathbf{\Omega}, E)$ is a incoming source term that can represent either the vacuum, incoming side source, or reflective boundary conditions given in equation (35).

Due to the highly localised nature of the NURBS basis functions the integrals over the domain can be split into a summation of integrals over the knot spans within patches. This leads to an assembly process similar to the one typically seen in the FE method. Each knot span can be visited and a local dense bilinear form computed. The global linear system of equations is then assembled using the geometric connectivity information. The final IGA discretised weak form is given by:

$\underline{\mathbf{\Omega}_m \cdot \mathbf{n} < 0}$:

$$\sum_{i=1}^{N} d_{i,m} \sum_{p=1}^{P} \sum_{e=1}^{e_p} \int_{V_e} \left(\frac{1}{\sigma_t} (\mathbf{\Omega}_m \cdot \nabla R_i^q)(\mathbf{\Omega}_m \cdot \nabla R_j^q) + \sigma_t R_i^q R_j^q \right) d\mathbf{r} = \sum_{p=1}^{P} \sum_{e=1}^{e_p} \int_{V_e} \left(Q_m R_j^q - \frac{Q_m}{\sigma_t} (\mathbf{\Omega}_m \cdot \nabla R_j^q) \right) d\mathbf{r} - \sum_{p=1}^{P} \sum_{b=1}^{b_p} \int_{S_b} \left(|\mathbf{\Omega}_m \cdot \mathbf{n}| Z R_j^q \right) d\mathbf{r}_s, \tag{49}$$

$\underline{\mathbf{\Omega}_m \cdot \mathbf{n} > 0}$:

$$\sum_{i=1}^{N} d_{i,m}\Bigg[\sum_{p=1}^{P}\sum_{e=1}^{e_p}\int_{V_e}\left(\frac{1}{\sigma_t}(\mathbf{\Omega}_m\cdot\nabla R_i^q)(\mathbf{\Omega}_m\cdot\nabla R_j^q)+\sigma_t R_i^q R_j^q\right)d\mathbf{r}-\sum_{p=1}^{P}\sum_{b=1}^{b_p}\int_{S_b}\left(|\mathbf{\Omega}_m\cdot\mathbf{n}|R_i^q R_j^q\right)d\mathbf{r}_s\Bigg]$$
$$=\sum_{p=1}^{P}\sum_{e=1}^{e_p}\int_{V}\left(Q_m R_j^q-\frac{Q_m}{\sigma_t}(\mathbf{\Omega}_m\cdot\nabla R_j^q)\right)d\mathbf{r},\quad \text{for } m=1,\ldots,M \tag{50}$$

where P is the number of patches in the domain, e_p is the number of knot spans in patch p, b_p is the number of knot spans on the external boundary of patch p, V_e is the volume of knot span e, and S_b is the external surface of knot span b. Equations (49) & (50) are the IGA-S_N-SAAF equations for the incoming and outgoing angles.

5. Numerical results

In this section the results of several test problems are explored. These include IGA discretisations compared to FE based discretisations and comparing the SAAF equation with the first-order neutron transport equation and the EP formulation.

The continuous IGA SAAF spatial discretisation method developed in this paper has been implemented with a Fortran code called ICARUS (Isogeometric Continuous self-Adjoint Radiation Using Splines). ICARUS is used to generate the SAAF-S_N results presented in this paper. The code is also capable of performing FE calculations and is used here to generate the FE results. This ensures that exactly the same solvers and convergence criteria are used for both IGA and FE solutions. Inferno is a first-order neutron transport code with local refinement capabilities [36, 37, 38]. It is a discontinuous IGA discrete ordinate (S_N) code and is used in this paper to generate reference solutions to a number of nuclear reactor physics verification benchmark test cases.

5.1. MMS: Gaussian modulated tensor product of trigonometric functions

The method of manufactured solutions (MMS) [57] is used here to investigate the rates of convergence of the IGA discretised SAAF equation for different orders of basis function. The function used to generate the source terms for the SAAF equation is a Gaussian function that is modulated in each direction using a high frequency trigonometric function:

$$f(x,y) = Cx(x-1)y(y-1)\exp\left(-(x-0.5)^2-(y-0.5)^2\right)\sin(nx)\sin(my) \tag{51}$$

where each term is chosen to ensure that the solution has the following properties:

- $x(x-1)y(y-1)$: enforces homogeneous Dirichlet boundaries on the unit square.
- $C\exp\left(-(x-0.5)^2-(y-0.5)^2\right)$: to make the solution smooth and infinitely differentiable.
- $\sin(nx)\sin(my)$: adds oscillations in both directions. This ensures that higher-order basis functions cannot trivially represent the solution.

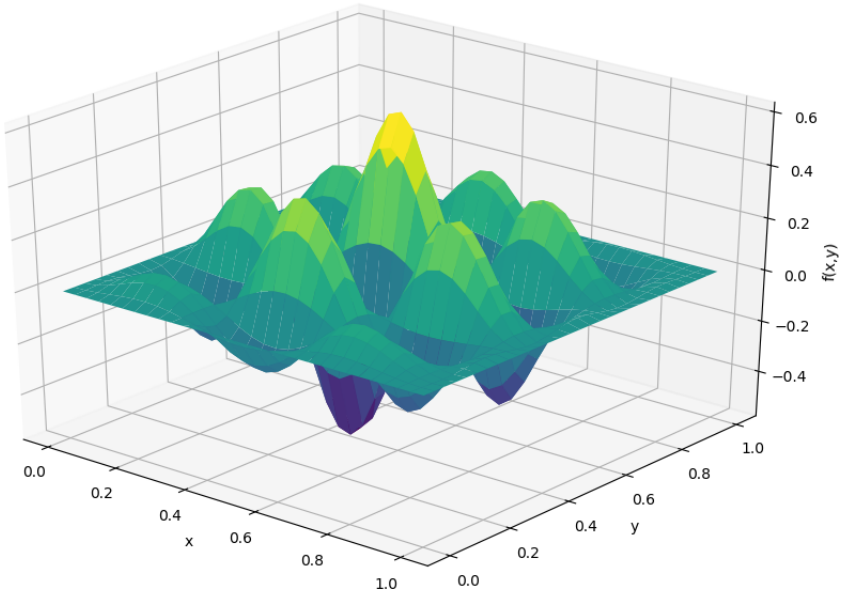

Figure 2: Example MMS function, $C = 10, m = 20, n = 10$

An example of this function can be seen in figure 2. The function $f(x, y)$ is substituted into the LHS of equation (11) and the remaining terms are taken as a source term $S(x, y, \mathbf{\Omega})$. This source term is then used on the RHS of the SAAF equation which is discretised using IGA with NURBS basis functions.

The convergence plot of the L_2-error in the solution computed using S_{20} IGA SAAF is shown in figure 3. The solution of the linear system of equations formed from the spatial and angular discretisation of the SAAF equation was performed using the incomplete Cholesky factorisation preconditioned conjugate gradient (ICC-PCG) algorithm implemented within PETSc using a iterative convergence tolerance of 10^{-13} for each angle. The solution algorithm was terminated when the magnitude of the residual in the scalar neutron flux was less than 10^{-10}. Basis functions of order one through six have been used and the theoretical order of convergence for degree p basis functions is $O(p + 1)$.

The order of convergence of all basis functions is limited initially until a sufficient spatial resolution has been achieved to allow the solution to capture the oscillations in expression (51). Once the level of discretisation is sufficient to capture the oscillatory behaviour, all solutions achieve an order of convergence close to the theoretical one. One exception to this is the highly refined $p = 6$ solution where the rate of convergence begins to decrease as the error in the solution begins to approach the convergence tolerance of the scalar neutron flux.

5.2. The IAEA swimming pool nuclear reactor physics verification benchmark test case

The IAEA swimming pool nuclear reactor physics verification test case was first defined in a IAEA report by J. Stepanek [58]. The problem is relatively insensitive to approximation in angle beyond a certain point [59]. The insensitivity to angular resolution can be seen in table 1 where the K_{eff} has been calculated using a discontinuous Galerkin IGA discrete ordinate (S_N)

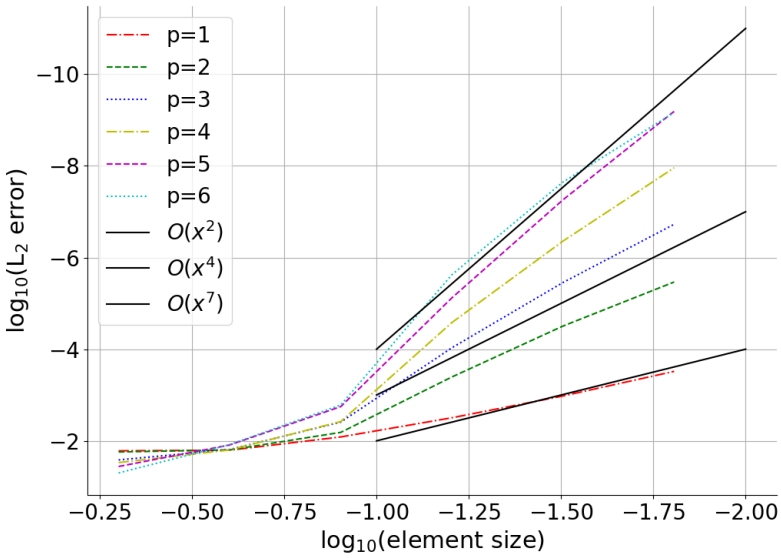

Figure 3: Spatial convergence plots of MMS verification test case

code, called Inferno, for different orders of angular quadrature with similar levels of spatial refinement. For this reason the IAEA swimming pool problem has been selected to explore the spatial convergence of the IGA discretised SAAF equation when compared to a FE discretisation. Furthermore, the problem itself is numerically challenging due to some regions being optically thick and the difference in order of magnitude between volume averaged scalar neutron fluxes in neighbouring regions. In this paper both an extraneous (fixed) and a fission source version of the IAEA swimming pool problem are considered. The geometry and macroscopic neutron cross-section data are presented in figure 4 and tables 2 & 3. The reference results for each problem were calculated using the Inferno code with roughly 1,200,000 quadratic elements per calculation and using S_{10} Legendre-Chebyshev quadrature. The reference quantity of interest (QoI) for the criticality problem is K_{eff} = 1.008875 and for the extraneous (fixed) source problem the volume averaged scalar neutron flux in each region is presented in table 4.

S_N	Number of elements	K_{eff}
8	1,199,569	1.0088657332
10	1,199,554	1.0088746303
20	1,199,560	1.0088852053
40	1,199,569	1.0088878513

Table 1: K_{eff} for various discrete ordinate (S_N) orders as calculated by Inferno for the IAEA swimming pool nuclear reactor physics benchmark.

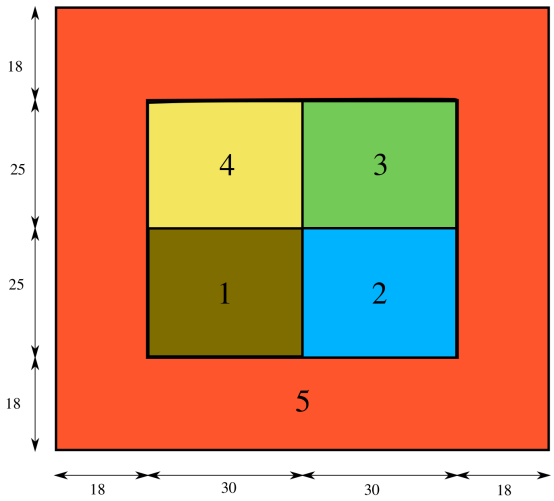

Figure 4: Geometry and region numbers for the IAEA swimming pool nuclear reactor physics verification test case. Vacuum boundary condition are prescribed on all boundaries of the solution domain.

Figure 5 shows the error in the K_{eff} for S_{10} quadratic IGA and FE solutions when compared to S_{20} Inferno for the fission source problem. The IGA solution always preserves the geometry (volume and surface area) exactly for geometries that can be represented by NURBS basis functions. However, due to the Cartesian geometry nature of the problem the FE method also preserves geometry (volume and surface area) of all regions.

It is seen that for the same number of dof the K_{eff} calculated using the IGA method is more accurate than the K_{eff} calculated using FEs. This is due to the high-order continuity of the NURBS basis over element boundaries within a NURBS patch. In this case they are C^1 continuous over element boundaries within a NURBS patch, whereas the FE basis functions are C^0 over element boundaries.

Plots of the error in the region averages for the extraneous (fixed) source problem are shown in figure 6. The same general behaviour can be observed, that is fewer dof are needed to reduce the error by a prescribed amount when using quadratic IGA compared to quadratic FEs. In particular, the error in the FE solution is about half an order of magnitude larger than the error in the IGA solution.

5.3. Seven-group, bare UO_2 fuel pin nuclear reactor physics verification benchmark test case

This seven-group, eigenvalue (K_{eff}), nuclear reactor physics verification benchmark test case consists of a two-dimensional UO_2 bare fuel pin of radius 0.54 cm with prescribed vacuum boundary conditions. The seven-group macroscopic neutron cross-section data for this verification test case are taken from the OECD/NEA C5G7 nuclear reactor physics benchmark for the UO_2 fuel-clad material [60]. The geometry for this verification test case is a modified version of a pincell from the two-dimensional OECD/NEA C5G7 quarter core test case. The fuel pin has the same dimensions as the original pincell but the moderating material has been removed. The modified bare fuel pin geometry is shown in figure 7. This benchmark has been specifically

Region	Macroscopic neutron cross-section data (cm^{-1})		
	σ_t	σ_s	$\nu\sigma_f$
1	0.6	0.53	0.079
2	0.48	0.20	0.0
3	0.70	0.66	0.043
4	0.65	0.50	0.0
5	0.90	0.89	0.0

Table 2: One-group macroscopic neutron cross-section data for the eigenvalue (K_{eff}) IAEA swimming pool nuclear reactor physics verification test case.

Region	1	2	3	4	5
Neutron source strength ($cm^{-3}.s^{-1}$)	1.0	0.0	1.0	0.0	0.0

Table 3: Extraneous (fixed) neutron source strengths for the fixed source IAEA swimming pool nuclear reactor physics verification test case.

Region	Volume averaged scalar neutron flux ($cm^{-2}.s^{-1}$)
1	11.9569693948
2	0.54057779903
3	19.1960438341
4	0.83475246098
5	1.52653294652

Table 4: Reference volume averaged scalar neutron flux solutions for the extraneous (fixed) source IAEA swimming pool nuclear reactor physics verification test case. These solutions were generated using the Inferno code.

designed to illustrate the effects of geometrical discretisation errors on the numerical accuracy and rate of convergence of the solution. The problem is solved using S_2 triangular Legendre-Chebyshev quadrature. The reference solution used is a highly refined sixth order IGA solution with K_{eff} = 7.30533835E^{-003}. The convergence plots of the IGA and volume preserved FEs are shown in figure 8.

It can be seen that for both sets of FE calculations the rate of convergence is limited by the rate of decrease of geometric error. In the non-volume preserved FE solution the errors in surface area, volume, and the total geometric error have been plotted and it can be observed that the rate of convergence of all solutions is limited to the rate of decrease in geometric error. Similar behaviour can be seen in the volume preserved FE solutions. Here the error in the surface area is slightly higher, however the error in volume is zero. This is due to the fact that the nodes on the surface are being pushed out by different amounts for different numbers of elements in order to maintain the volume of the geometry. Therefore, the surface polygon circumscribes the true circular geometry. In the non-volume preserved case the polygon inscribes the geometry.

The errors in the non-volume preserved and volume preserved FE solutions differ by roughly two orders of magnitude for higher-order basis functions. Therefore, the larger error in the

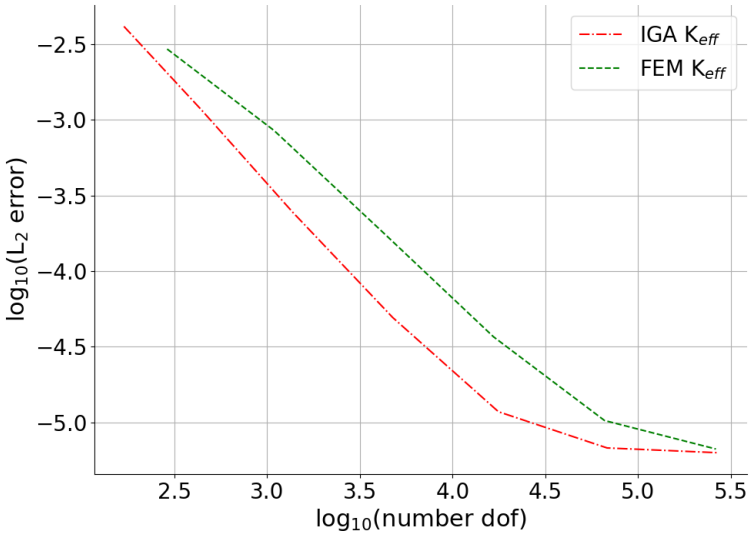

Figure 5: Error in the K_{eff} for the eigenvalue IAEA swimming pool reactor physics benchmark. Both the IGA and FE use quadratic basis functions and a S_{10} angular quadrature set. Both solutions were computed using ICARUS where a triangular Legendre-Chebyshev discrete ordinate angular quadrature has been used. The results are compared to the reference solution provided by an Inferno S_{20} solution.

surface area incurred by preserving volume would appear to be worthwhile. The difference between the volume preserved FE and IGA results are even greater. This is mainly due to the fact that the rate of convergence of the IGA solution is not limited by the geometric approximation as the geometry is represented exactly for all levels of refinement. Further accuracy in the IGA solution is obtained due to the high inter-element continuity of the NURBS basis functions within a NURBS patch, as was demonstrated in section 5.2.

A more in depth study of the effects of higher-order isoparametric FE basis functions on the surface and volume errors has been performed [61, 62]. Furthermore, the comparison of these methods to IGA has also been extensively studied as well [35].

5.4. OECD/NEA, seven-group, two-dimensional (2D) C5G7 nuclear reactor physics verification benchmark test case

The OECD/NEA C5G7 verification test case is a two-dimensional (2D), seven-group, heterogeneous, quarter core nuclear reactor physics benchmark used by the OECD/NEA and code developers as a means of verifying the implementation and assessing the accuracy of deterministic neutron transport codes. The material composition can be seen in figure 9 and the macroscopic neutron cross-section data for the benchmark can be found in Appendix A of the benchmark specification [60].

Figures 10a, 10b, & 10c show the neutron scalar flux profiles for the C5G7 quarter core verification test case. It can be seen that the fast and epithermal neutrons are born in the fuel regions. As they are transported through the domain down scattering causes a drop in the fast

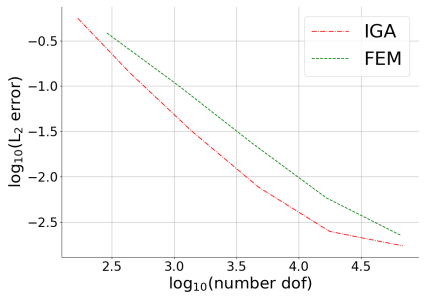

(a) Region 1

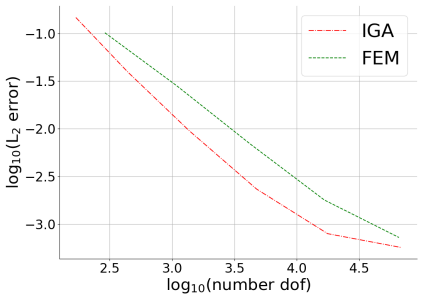

(b) Region 2

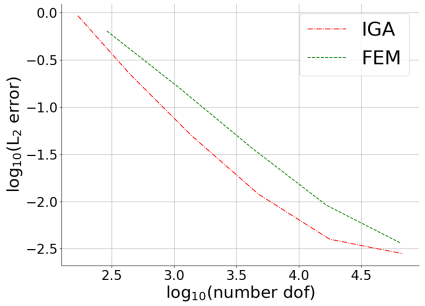

(c) Region 3

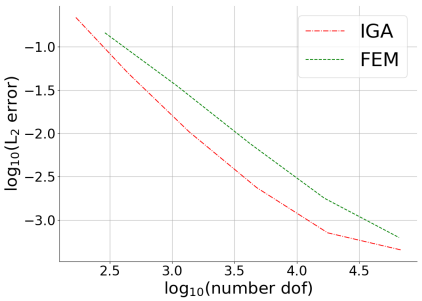

(d) Region 4

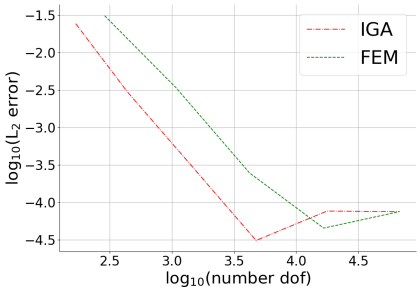

(e) Region 5

Figure 6: Error in the volume averaged scalar neutron flux for the extraneous (fixed) source IAEA swimming pool reactor physics benchmark in each region computed by ICARUS using quadratic IGA and quadratic FEs with an S_{10} angular quadrature. The reference solutions were produced using the discontinuous Galerkin IGA S_N code Inferno.

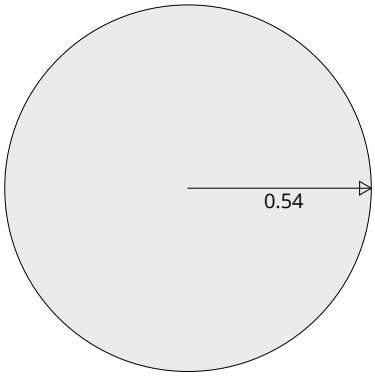

Figure 7: Geometry for the seven-group, bare UO_2 fuel pin eigenvalue (K_{eff}) nuclear reactor physics verification benchmark test case. Vacuum boundary conditions have been prescribed on the boundary of the bare UO_2 fuel pin.

and epithermal scalar neutron fluxes as the neutron energy is attenuated. As neutrons enter the reflector region from the fuel region there is a large spike in the thermal scalar neutron flux caused by the large scattering cross-section causing any fast neutrons to become thermalised.

Several results are presented for comparison. First are the solutions of the benchmark from the first-order neutron transport IGA discrete ordinate (S_N) code Inferno. The results presented are from a reference solution with $2,164,032$ quadratic elements for the whole geometry. and S_8 angular discretisation. The eigenvalue was converged up to 10^{-11} and can be found in Owens' paper [36]. Second are the results from the even-parity S_N code CRONOS2 [63]. These results were discretised using linear triangular FEs that give $24,804$ degrees of freedom for the entire geometry. An S_8 angular discretisation was used and these results can be found in the OECD/NEA C5G7 benchmark book [60]. Finally, results from ICARUS using quadratic basis functions are presented. Tables 5, 6, 7 and 8 present the errors in several quantities of interest (QoI) for CRONOS2 and ICARUS against Inferno. It is assumed that the CRONOS2 FE mesh is mass preserving as ICARUS ran a similar FE problem with no mass preservation and the error in the K_{eff} was significantly greater.

Number of degrees of freedom (dof)	K_{eff} (pcm)	Maximum pin power (%)	Minimum pin power (%)	Inner UO_2 assembly (%)	Outer UO_2 assembly (%)	MOX assembly (%)
24804	58	0.0049	-0.041	0.0031	-0.0041	-0.0023

Table 5: Error in CRONOS2 solution compared to the Inferno C5G7 reference result. The K_{eff} is converged to 10^{-6}. The particular S_8 angular quadrature set is unknown.

Tables 5, 6, and 7 show the errors in various quantities of interest (QoI). The solution algorithm has been terminated when the eigenvalue for successive iterations differs by less than 10^{-6}. It can be observed that the IGA solution is superior to FE solution. This is due, in part, to the quadratic basis functions used and also to the exact representation of the surface area and volume of each pin, whereas the FE solution only preserves fuel pin volume. While the coarsest ICARUS solve has more dof than the CRONOS2 solve the number of dof per pincell is the

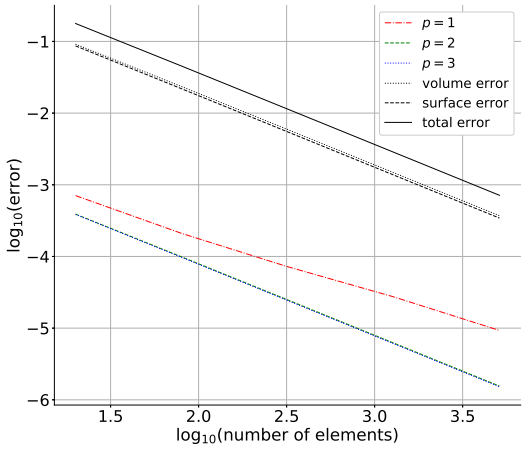

(a) Non-volume preserved FEs

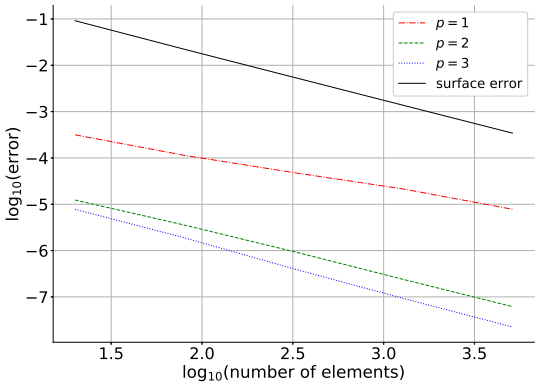

(b) Volume preserved FEs

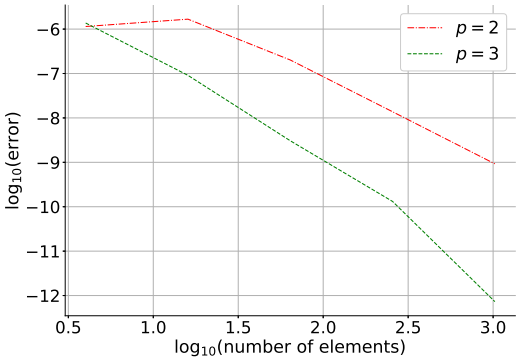

(c) IGA

Figure 8: Error in the K_{eff} for the bare fuel pin problem for varying levels of spatial and polynomial refinement within a NURBS patch. All results calculated using ICARUS .

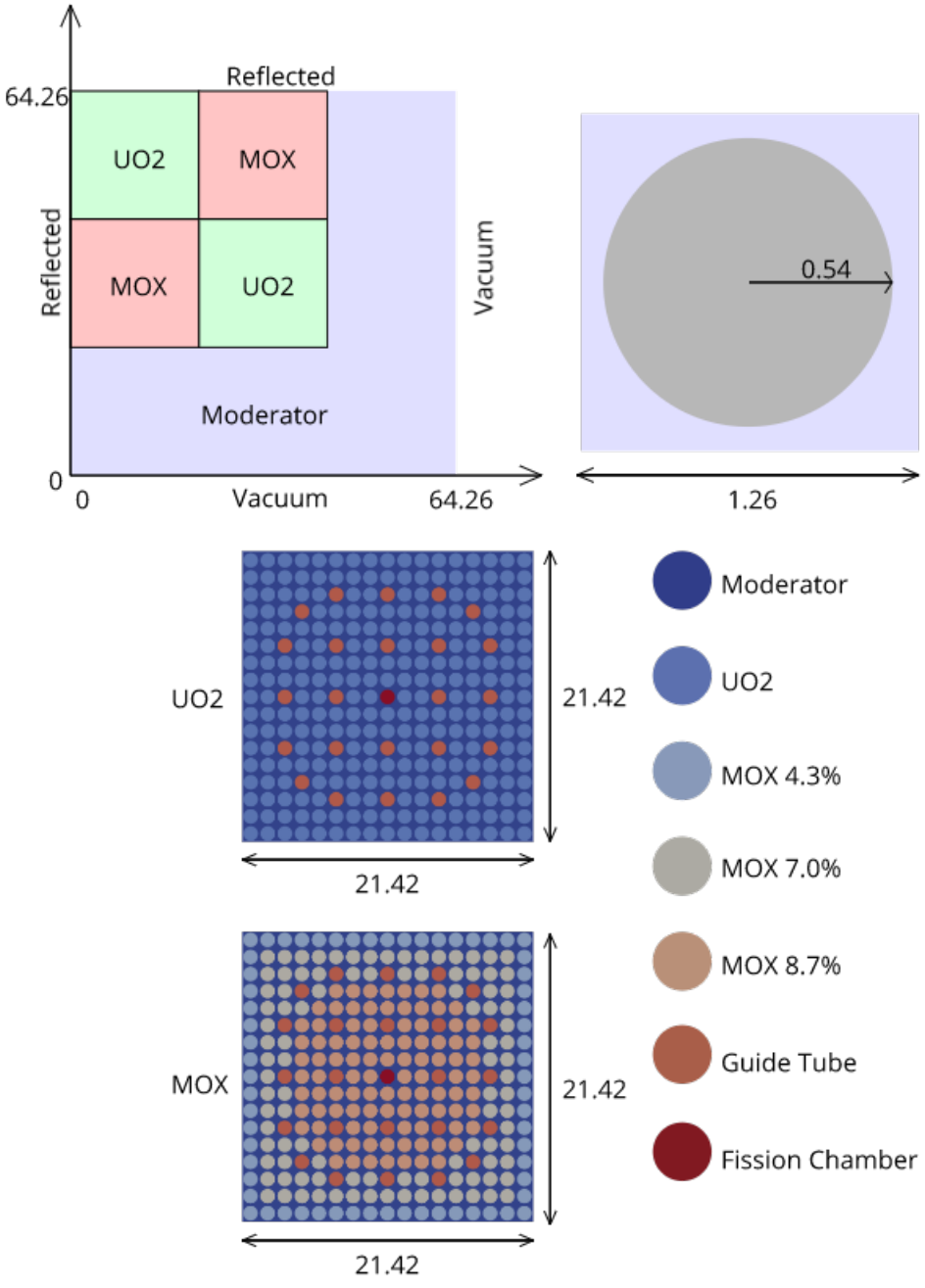

Figure 9: Geometry specification for the OECD/NEA C5G7 benchmark.

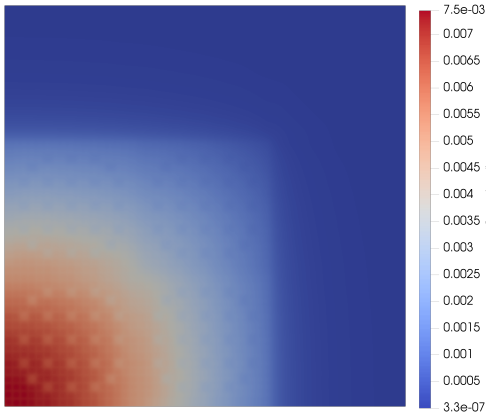

(a) Group 1 (fast scalar neutron flux with units $cm^{-2}.s^{-1}$)

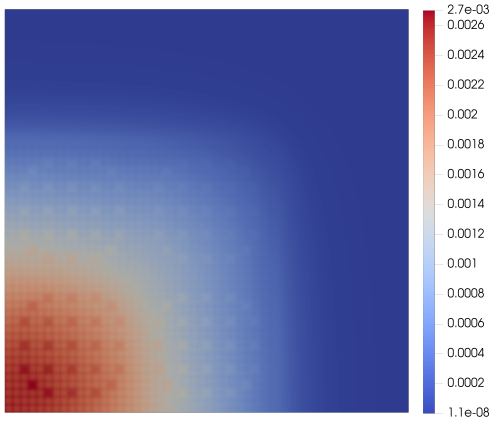

(b) Group 4 (epithermal scalar neutron flux with units $cm^{-2}.s^{-1}$)

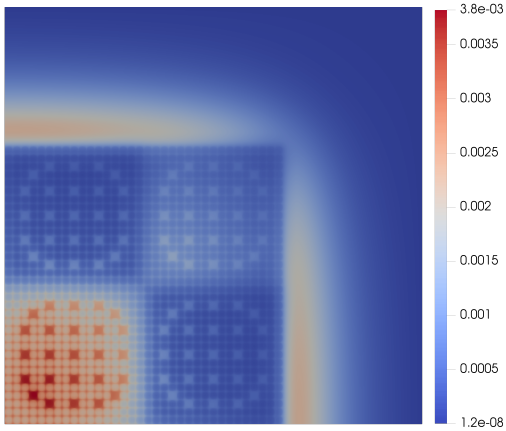

(c) Group 7 (thermal scalar neutron flux with units $cm^{-2}.s^{-1}$)

Figure 10: Scalar neutron flux profiles for the OECD/NEA C5G7 quarter core nuclear reactor physics verification test case for several energy groups. The scalar neutron flux is normalised to unit fission source.

Number of degrees of freedom (dof)	K_{eff} (pcm)	Maximum pin power (%)	Minimum pin power (%)	Inner UO_2 assembly (%)	Outer UO_2 assembly (%)	MOX assembly (%)
29105	52	0.0030	-0.0177	0.0016	-0.0014	-0.0014

Table 6: Error in ICARUS solution compared to Inferno C5G7 reference result. The K_{eff} has been converged to 10^{-6} and a triangular Legendre-Chebyshev S_8 angular quadrature set has been used.

Number of degrees of freedom (dof)	K_{eff} (pcm)	Maximum pin power (%)	Minimum pin power (%)	Inner UO_2 assembly (%)	Outer UO_2 assembly (%)	MOX assembly (%)
29105	57	0.0027	-0.0179	0.0014	-0.0014	-0.0012

Table 7: Error in ICARUS solution compared to Inferno C5G7 reference result. The K_{eff} has been converged to 10^{-6} and a level-symmetric S_8 angular quadrature set has been used.

Number of degrees of freedom (dof)	K_{eff} (pcm)	Maximum pin power (%)	Minimum pin power (%)	Inner UO_2 assembly (%)	Outer UO_2 assembly (%)	MOX assembly (%)
29105	311	-0.0051	-0.0154	-0.0039	0.0012	0.0040
65332	302	-0.0089	-0.0014	-0.0060	0.0025	0.0062
181136	296	-0.0083	0.00053	-0.0057	0.0026	0.0057

Table 8: Error in ICARUS solution compared to the Monte-Carlo C5G7 reference solution found in the benchmark specification [60]. The K_{eff} has been converged to 10^{-7} and a S_8 triangular Legendre-Chebyshev angular quadrature set has been used.

same. The ICARUS IGA mesh has slightly more dof in the water near the boundaries than the CRONOS2 FE mesh. Therefore, the extra dof in the IGA mesh should affect the pin powers minimally. Furthermore, it can be seen from figure 10 that the flux profiles in the water near the boundaries are relatively flat so fewer dof are required to represent the solution here.

Whilst the pin power results for the ICARUS solution in table 7 are clearly more accurate than the CRONOS2 solution, the difference in the two K_{eff} values is only 1 pcm. The angular quadrature set used by CRONOS2 is not known to the authors so, in an effort to investigate how much of a difference angular quadrature sets might make, tables 6 and 7 show the errors in ICARUS calculations where the only difference is the use of triangular Legendre-Chebyshev (LCT) and level-symmetric set (LSS) quadrature sets. Both quadrature sets result in the same number of angular unknowns. It can be seen that there is a difference of 5pcm in the K_{eff} whilst the pin power errors change minimally. Therefore, we conclude that the small difference seen between the K_{eff} for the CRONOS2 and ICARUS results could be caused by the use of different angular quadrature sets.

Table 8 shows the errors in various QoI calculated from IGA-SAAF solutions of the OECD/NEA C5G7 verification test case using ICARUS. The results have been compared against the reference Monte-Carlo solution from the OECD/NEA C5G7 benchmark specification [60]. Three levels of discretisation are presented. The coarsest mesh is identical to the one used in tables 6 & 7

and the two finer meshes are the result of refining each patch once or twice respectively in each parametric direction. The tolerance for the relative change in K_{eff} is 10^{-7} to make sure that errors in the QoI were not caused by a lack of convergence.

It can be seen that most quantities of interest are converging slowly to the reference solution, whilst others appear to diverge. It is postulated that the reason for the slow convergence of some QoI, the divergence of other QoI, and the large pcm difference in the K_{eff} is caused by the low angular quadrature set used. Furthermore, there will be an error introduced into the S_8-IGA solution due to the ray effect. These errors are not present in the reference Monte-Carlo solution and cause a discrepancy. Indeed, the pcm error between the K_{eff} from the finest solution in table 8 and the highly refined S_8 first-order transport reference solution generated using Inferno is only 37pcm.

6. Conclusion

In this paper a maximum principle compatible with source iteration based upon the SAAF form of the neutron transport equation was presented. It was shown to be mathematically equivalent to a Bubnov-Galerkin discretisation of the weak form of the SAAF neutron transport equation. This variational derivation provides a rigorous mathematical justification for the use of the first-order form of the neutron transport equation as a boundary condition for the outgoing angular flux on the boundary of the solution domain. The SAAF equation was spatially discretised using isogeometric analysis (IGA) with non-uniform rational B-spline (NURBS) test and trial functions. A method of manufactured solutions (MMS) verification test case demonstrates that this spatial discretisation yields close to the theoretical order of convergence for several orders of basis functions. Several extraneous (fixed) source and eigenvalue (K_{eff}) nuclear reactor physics verification benchmark test cases comparing FE and IGA spatial discretisations of the SAAF equation were performed. It was demonstrated that in the case where the geometry could be represented exactly by both IGA and FE basis functions that the IGA spatial discretisation was more accurate per dof. This improvement in spatial accuracy, using the IGA method, was due to the high inter-element continuity of the NURBS basis functions within a NURBS patch. Furthermore, in the case where the FE method is unable to exactly represent the geometry it was demonstrated that this geometric error limits the rate of convergence of the overall solution.

The OECD/NEA, seven-group, two-dimensional C5G7 quarter core nuclear reactor physics verification benchmark problem was solved using a discrete ordinate (S_N) IGA spatial discretisation of the SAAF equation. The IGA SAAF solutions were compared against a second-order even-parity (EP) solution from the CRONOS2 FE code. This comparison was performed on meshes with similar numbers of dof and shows that the IGA solution was more accurate spatially than a similar FE solution. Furthermore, the effect of discrete ordinate (S_N) angular quadrature sets on the solution was also investigated.

Overall the IGA spatial discretisation method seems a promising numerical discretisation scheme, especially for second-order forms of the neutron transport equation. The ability to solve nuclear reactor physics problems using the same geometrical representation utilised in commercial CAD software has great potential to reduce the time required to set up complex geometry neutron transport problems. Moreover, the ability to exactly model both the volume and surface area, as well as having higher-order continuity within a NURBS patch, leads to improved convergence over conventional FE based discretisation schemes.

Further research is required to extend the IGA SAAF method to general three-dimensional (3D) nuclear reactor physics and radiation shielding problems as well as to incorporate energy-

dependent spatially adaptive IGA algorithms (with appropriate dual weighted residual or goal based error measures) for the SAAF form of the neutron transport equation. The spatial adaptivity is particularly beneficial for the IGA method as the geometry is always preserved even on the coarsest spatial refinement. Therefore, such a spatially adaptive IGA method always preserves the volume and surface area throughout the solution domain when the geometry is defined using NURBS. Furthermore, it would be interesting to perform a full comparison of the IGA discretised SAAF equation against the IGA discretised first-order transport equation including detailed comparisons of solution accuracy, storage requirements, and computational time required to solve the system of linear equations.

Acknowledgements

C. Latimer would like to acknowledge the Engineering and Physical Sciences Research Council (EPSRC) through the Doctoral Training Award (DTA) PhD scheme and their knowledge transfer secondment (KTS) programme (EPSRC impact acceleration award grant reference number: EP/R511547/1). C. Latimer also acknowledges the industrial support of Rolls-Royce. C. Latimer would also like to thank John Ferguson for providing diagrams of the OECD/NEA C5G7 test case. M.D. Eaton and J. Kópházi would like to thank the EPSRC for their support through the following grants: Adaptive Hierarchical Radiation Transport Methods to Meet Future Challenges in Reactor Physics (EPSRC Grant No.: EP/ J002011/1) and RADIANT: A Parallel, Scalable, High Performance Radiation Transport Modelling and Simulation Framework for Reactor Physics, Nuclear Criticality Safety Assessment and Radiation Shielding Analyses (EPSRC Grant No.: EP/K503733/1). Finally, the authors would like to thank the high performance computing (HPC) service support team at Imperial College London.

References

[1] V. S. Vladimirov. Mathematical problems in the one-velocity theory of particle transport. Technical Report AECL-1661, Atomic Energy of Canada Ltd., Chalk River, Ontario, January 1963.

[2] G. C. Pomraning and M. Clark. The Variational Method Applied to the Monoenergetic Boltzmann Equation, Part II. *Nuclear Science and Engineering*, 16:155–164, 1963.

[3] W. R. Martin and J. J. Duderstadt. Finite Element Solutions of the Neutron Transport Equation with Applications to Strong Heterogeneities. *Nuclear Science and Engineering*, 62:371–390, 1976.

[4] C. C. Pain, M. D. Eaton, R. P. Smedley-Stevenson, A. J. H. Goddard, M. D. Piggot, and C. R. E. de Oliveira. Space-time streamline upwind Petrov-Galerkin methods for the Boltzmann transport equation. *Computer Methods in Applied Mechanics and Engineering*, 195:4334–4357, 2006.

[5] C. C. Pain, M. D. Eaton, R. P. Smedley-Stevenson, A. J. H. Goddard, M. D. Piggott, and C. R. E. de Oliveira. Steamline upwind Petrov-Galerkin methods for the steady-state Boltzmann transport equation. *Computer Methods in Applied Mechanics and Engineering*, 195:4448–4472, 2006.

[6] W. H. Reed. TRIANGULAR MESH DIFFERENCE SCHEMES FOR THE TRANSPORT EQUATION. Technical Report LA-4769, Los Alamos Scientific Lab, 1971.

[7] W. H. Reed and T. R. Hill. Triangular mesh methods for the neutron transport equation. Technical Report LA-UR-73-479, Los Alamos National Laboratory, 1973.

[8] J. E. Morel, B. T. Adams, T. Noh, J. M. McGhee, T. M. Evans, and T. J. Urbatsch. Spatial discretizations for self-adjoint forms of the radiative transfer equations. *Journal of Computational Physics*, 214:12–40, 2006.

[9] M. Hanus and R. G. McClarren. On the use of symmetrized transport equation in goal-oriented adaptivity. *Journal of Computational and Theoretical Transport*, 0(0):1–20, 2016.

[10] J. N. Reddy. *Energy Principles and Variational Methods in Applied Mechanics*. John Wiley & Sons, 2017.

[11] J. E. Morel and J. M. McGhee. A self-adjoint angular flux equation. *Nuclear Science and Engineering*, 132:312–325, 1999.

[12] J. Hansen, J. Peterson, J. Morel, J. Ragusa, and Y. Wang. A Least-Squares Transport Equation Compatible with Voids. *Journal of Computational and Theoretical Transport*, 43:374–401, 2014.

[13] V. M. Laboure, R. G. McClarren, and Y. Wang. Globally Conservative, Hybrid Self-Adjoint Angular Flux and Least-Squares Method Compatible with Voids. *Nuclear Science and Engineering*, 185:294–306, February 2017.

[14] Y. Wang, H. Zhang, and R. C. Matrineau. Diffusion acceleration schemes for self-adjoint angular flux formulation with a void treatment. *Nuclear Science and Engineering*, 176:201–225, 2014.

[15] W. Zheng, R. G. McClarren, and J. E. Morel. An Accurate Globally Conservative Subdomain Discontinuous Least-Squares Scheme for Solving Neutron Transport Problems. *Nuclear Science and Engineering*, 189:259–271, 2018.

[16] R. T. Ackroyd. Least-Squares Derivation of Extremum and Weighted-Residual Methods for Equations of Reactor Physics - I. The First-Order Boltzmann Equation and a First-Order Initial-Value Equation. *Annals of Nuclear Energy*, 10:65–99, 1983.

[17] J. M. McGhee, R. M. Roberts, and J. E. Morel. The DANTE Boltzmann transport solver: An unstructured mesh, 3-D, spherical harmonics algorithm compatible with parallel computer architectures. Technical Report LA-UR–97-1031, Los Alamos National Lab, 1997.

[18] J. L. Liscum-Powell, A. K. Prinja, J. E. Morel, and L. J. Lorence. Finite element solution of the self-adjoint angular flux equation for coupled electron-photon transport. *Nuclear Science and Engineering*, 142:270–291, 2002.

[19] W. C. Fan, C. F. Drumm, and J. L. Powell. Discrete ordinates approximations to the first and second-order radiation transport equations. Technical Report SAND2002-1880, Sandia National Laboratory, 2002.

[20] R. T. Ackroyd. The self-adjoint angular flux equation for neutron transport: I - the maximum principle, and its potential for self-adaptive synthesis of solutions. *Annals of Nuclear Energy*, 33:1271–1296, 2006.

[21] L. Cao and H. Wu. A spherical harmonics - finite element discretization of the self-adjoint angular flux neturon transport equation. *Nuclear Engineering and Design*, 237:2232–2239, 2007.

[22] Y. Wang and F. N. Gleicher. Revisit boundary conditions for the self-adjoint angular flux formulation. In *PHYSOR 2014 - The Role of Reactor Physics toward a Sustainable Future*, Kyoto, Tokyo, September 2014.

[23] S. Schunert, Y. Wang, R. Matrineau, and M. D. DeHart. A new mathematical adjoint for the modified SAAF-S_N Equations. *Annals of Nuclear Energy*, 75:340–352, 2015.

[24] Y. Wang, M. D. DeHart, D. R. Gaston, F. N. Gleicher, R. C. Martineau, J. Ortensi, J. W. Peterson, and S. Schunert. Convergence study of rattlesnake solutions for the two-dimensional C5G7 MOX benchmark. In *ANS M&C2015 - Joint International Conference on Mathematics and Computation (M&C), Supercomputing in Nuclear Applications (SNA) and the Monte Carlo (MC) Method*. Nashville, TN, USA, April 2015.

[25] D. Gaston, C. Newman, G. Hansen, and D. Lebrun-Grandié. Moose: A parallel computational framework for coupled systems of nonlinear equations. *Nuclear Engineering and Design*, 239:1768–1778, 2009.

[26] R. T. Ackroyd. *Finite Element Methods for Particle Transport: applications to reactor and radiation physics*. John Wiley & Sons, 1997.

[27] E. E. Lewis. Second order neutron transport methods. In *Nuclear Computational Science: A Century in Review*. Springer, 2010.

[28] C. Drumm. Spherical harmonics (P_N) methods in the sceptre radiation transport code. In *ANS M&C2015 - Joint International Conference on Mathematics and Computation (M&C), Supercomputing in Nuclear Applications (SNA) and the Monte Carlo (MC) Method*, Nashville, TN, USA, April 2015. American Nuclear Society.

[29] N. Nahavandi, A. Minuchehr, A. Zolfaghari, and M. Abbasi. Spatially adaptive hp refinement approach for P_N neutron transport equation using spectral element method. *Annals of Nuclear Energy*, 85:1066–1076, 2015.

[30] E. H. Mund. Spectral element solutions for the P_N neutron transport equations. *Computers & Fluids*, 43:102–106, 2011.

[31] A. Barbarino, S. Dulla, E. H. Mund, and P. Ravetto. The spectral element method for static neutron transport in A_N approximation. Part I. *Annals of Nuclear Energy*, 53:372–380, 2013.

[32] A. Barbarino, S. Dulla, E. H. Mund, and P. Ravetto. The spectral element method for static neutron transport in A_N approximation. Part II. *Annals of Nuclear Energy*, 86:108–115, 2015.

[33] S. K. Hall, M. D. Eaton, and M. M. R. Williams. The application of isogeometric analysis to the neutron diffusion equation for a pincell problem with an analytic benchmark. *Annals of Nuclear Energy*, 49:160–169, 2012.

[34] J. Welch, J. Kópházi, A. R. Owens, and M. D. Eaton. A geometry preserving, conservative, mesh-to-mesh isogeometric interpolation algorithm for spatial adaptivity of the multigroup, second-order even-parity form of the neutron transport equation. *Journal of Computational Physics*, pages 129–146, August 2016.

[35] J. A. Welch, J. Kópházi, A. R. Owens, and M. D. Eaton. Isogeometric analysis for the multigroup neutron diffusion equation with applications in reactor physics. *Annals of Nuclear Energy*, 101:465–480, 2017.

[36] A. R. Owens, J. A. Welch, J. Kópházi, and M. D. Eaton. Discontinuous isogeometric analysis methods for the first-order form of the neutron transport equation with discrete ordinate (S_N) angular discretisation. *Journal of Computational Physics*, 315:501–535, 2016.

[37] A. R. Owens, J. A. Welch, J. Kópházi, and M. D. Eaton. An adaptive, hanging-node, discontinous isogeometric analysis method for the first-order form of the neutron transport equation with discrete ordinate (S_N) angular discretisation. *Computer Methods in Applied Mechanics and Engineering*, 318:215–241, 2017.

[38] A. R. Owens, J. Kópházi, J. A. Welch, and M. D. Eaton. Energy dependent mesh adaptivity of discontinous isogeometric discrete ordinate methods with dual weighted residual error estimators. *Journal of Computational Physics*, 335:352–386, 2017.
[39] T. J. R. Hughes, J. A. Cottrell, and Y. Bazilevs. Isogeometric analysis: CAD, finite elements, NURBS, exact geometry and mesh refinement. *Computer Methods in Applied Mechanics and Engineering*, 194:4135–4195, 2005.
[40] T. J. R. Hughes, J. A. Cottrell, and Y. Bazilevs. *Isogeometric Analysis: Toward Integration of CAD and FEA*. John Wiley and Sons, 2009.
[41] C. de Falco, A. Reali, and R. Vázquez. GeoPDE's : A research tool for Isogeometric Analysis of PDE's. *Advances in Engineering Software*, 42:1020–1034, 2011.
[42] C. Hofreither and S. Takacs. Robust multigrid for isogeometric analysis based on stable splittings of spline spaces. *SIAM Journal of Numerical Analysis*, 55(4):2004–2024, 2017.
[43] Y. Bazilevs, V. M. Calo, J. A. Cottrell, J. E. Evans, T. J. R. Hughes, S. Lipton, M. A. Scott, and T. W. Sederberg. Isogeometric analysis using T-splines. *Computer Methods in Applied Mechanics and Engineering*, 199:229–263, 2010.
[44] R. R. Hiemstra, F. Calabro, D. Schillinger, and T. J. R. Hughes. Optimal and Reduced Quadrature Rules for Tensor Product and Hierachically Refined Splines in Isogeometric Analysis. *Computer Methods in Applied Mechanics and Engineering*, 316:966–1004, 2017.
[45] L. Piegl and W. Tiller. *The NURBS Book 2nd edition*. Springer-Verlag, 1997.
[46] D. C. Thomas, M. A. Scott, J. A. Evans, K. Tew, and E. J. Evans. Bézier projection: A unified approach for local projection and quadrature-free refinement and coarsening of NURBS and T-splines with particular application to isogeometric design and analysis. *Computer Methods in Applied Mechanics and Engineering*, 284:55–105, 2015.
[47] F. Calabrò, G. Sangalli, and M. Tani. Fast Formation of Isogeometric Galerkin Matrices by Weighted Quadrature. *Computer Methods in Applied Mechanics and Engineering*, 316:606–622, 2017.
[48] J. A. Cottrell, A. Reali, Y. Bazilevs, and T. J. R. Hughes. Isogeometric analysis of structural vibrations. *Computer Methods in Applied Mechanics and Engineering*, 195:5257–5296, 2006.
[49] L. Piegl. On NURBS: A Survey. *IEEE Computer Graphics and Applications*, 11:55–71, 1991.
[50] N. Collier, D. Pardo, L. Dalcin, M. Paszynski, and V. M. Calo. The cost of continuity: A study of the performance of isogeometric finite elements using direct solvers. *Computer Methods in Applied Mechanics and Engineering*, 213-216:353–361, 2012.
[51] K. P. S. Gahalaut, J. K. Kraus, and S. K. Tomar. Multigrid methods for isogeometric discretization. *Computer Methods in Applied Mechanics and Engineering*, 253:413–425, 2013.
[52] L. Beirao da Veiga, D. Cho, L. F. Pavarino, and S. Scacchi. BDDC preconditioners for isogeometic analysis. *Mathematical Models and Methods in Applied Sciences*, 23(6):1099–1142, 2013.
[53] E. E. Lewis and W. F. Miller. *Computational Methods of Neutron Transport*. American Nuclear Society, Inc., La Grange Park, Illinois USA, 1993.
[54] R. T. Ackroyd. A Finite Element Method for Neutron Transport I. Some Theoretical Considerations. *Annals of Nuclear Energy*, 5:75–94, 1978.
[55] O. C. Zienkiewicz and K. Morgan. *Finite Elements & Approximation*. Dover Publications, 2006.
[56] J .T. Oden and J. N. Reddy. *An Introduction to the Mathematical Theory of Finite Elements*. Dover Publications, 1976.
[57] P. J. Roache. Code verification by the method of manufactured solutions. *Journal of Fluids Engineering*, 124:4–10, 2002.
[58] IAEA. Transport Theory and Advanced Reactor Calculations: final report of the six-year co-ordinated research programme by the international atomic energy agency. Technical Report IAEA-TECDOC-254, IAEA, 1981.
[59] J. Stepanek, T. Auerbach, and W. Haig. Calculation of Four Thermal Reactor Benchmark Problems in X-Y-Geometry. Technical Report 464, Federal Institute of Technology Zurich, 1982.
[60] E. E. Lewis, G. Palmiotti, T. A. Taiwo, M. A. Smith, and N. Tsoulfanidisowens. Benchmark on Deterministic Transport Calculations Without Spatial Homogenisation - A 2-D/3-D MOX Fuel Assembly Benchmark. *Nuclear Science*, 2003.
[61] J. Y. Moller and J. J. Lautard. MINARET, a Deterministic Neutron Transport Solver for Nuclear Core Calculations. In *International Conference on Mathematics and Computational Methods Applied to Nuclear Science and Engineering*, Rio de Janiro, Brazil, May 2011.
[62] J. Y. Moller. *Eléments finis courbes et accélération pour le transport de neutrons*. PhD thesis, 2012.
[63] F. Moreau, R. Sanchez, S. Santandrea, I. Zmijarevic, and E. Masiello. CRONOS2 and APOLLO2 results for the NEA C5G7 MOX benchmark. *Progress in Nuclear Energy*, 45(2-4):179–200, 2004.